SYNTHESIS OF IRON NANOPARTICLES MEDIATED BY CELLULOSE NANOCRYSTALS

SYNTHESIS OF IRON NANOPARTICLES MEDIATED BY CELLULOSE NANOCRYSTALS

by

MARIA XIMENA RUIZ-CALDAS, B. Chemical Engineering

A Thesis

Submitted to the School of Graduate Studies

in Partial Fulfillment of the Requirements

for the Degree

Master of Applied Science

McMaster University

MASTER OF APPLIED SCIENCE (2018) McMaster University

(Chemical Engineering) Hamilton, Ontario

TITLE: Synthesis of iron nanoparticles mediated by cellulose nanocrystals

AUTHOR: Maria Ximena Ruiz-Caldas

B. Chemical Engineering (Universidad Nacional de Colombia)

SUPERVISOR: Professor Charles François de Lannoy

NUMBER OF PAGES: xi, 84

…To my parents, my dog and my brother (in that order)…

Acknowledgments

First of all, I want to express my sincere gratitude to my supervisor Dr. Charles de Lannoy for accepting me as his master's student. There are no words to describe how grateful I am to Dr. de Lannoy for giving me the opportunity to be his first master's student. It is an honor to start my career in scientific research under his supervision. I am so grateful for his great patience, guidance, mentoring and for all the help that I get throughout my master's degree. I could not have asked for a better supervisor.

Part of my experiments were made at the Canadian Center for Electron Microscopy (CCEM). I am truly grateful to the staff at CCEM, especially with Dr. Carmen Andrei for her training and support during my microscopy sessions.

Thanks to Ms. Kristina Trollip, Ms. Michelle Whalen and Ms. Linda Ellis for helping me handle all the administrative work. Thanks to Mr. Paul Gatt, Mechanical Technician, for his assistance throughout my project

I am also very grateful to the undergraduate students that worked with me: Mr. Prabhjot Burmy, Ms. Beatrice Benigno, and Ms. Thabeisha Siva. Your contributions and hard work were very important to accomplish this thesis.

I am immensely grateful to Dr. Carla Abarca for all the help and support she gave me throughout this last year. This work was made because you were always here. Thank you for the countless hours of laughs, wisdom, and time spent with someone like me. I am quite sure that you will be an amazing mother, in the same way that you are an amazing friend.

I have to acknowledge Mr. Daniel Osorio (a.k.a. Osorio-Sama) for his help since the first months of my master's. Thanks for your friendship, your thoughtfulness, and for

always being there in such a good mood. I also have to mention Mr. Heera Marway for his support, guidance, and enthusiasm with research.

To every new friend I have been fortunate enough to meet and get to know at McMaster. To the Iranians: Amin, Amir, Reza, Hossein, Azadeh, and Sarah; thanks for the laughs, the stories, and for showing me your rich culture. To the Serbians (my Kurvas) Ilinka and Darko, for your particular sense of humor and all the advice you gave me (you guys are crazy!).

To the Latinos: Cristina, Fredy, Ana, Ana Laura, Andrés, Daniel (Tinajero), Alvaro, Israel, Oscar, and Azucena; thank you guys for all the laughs, memories and stories, and especially for being extraordinary friends

Thanks to Mr. Juan Pablo Jimenez and his family. You guys helped since the first day of my arrival to Canada. Thanks for letting me be part of such an amazing family. Thank for all you have done for me over these two years. I truly hope someday I will return you the favor.

Thanks to all my friends at the distance: To Lina Gelvez for always having a solution for every problem; to Karla Gil for being my adventure mate; to Andrés Amador for your humor and our nice chats; to Mia Barlow for your kindness and all the laughter; to Zulma Betancourt to listen to my stories; to Ame Hernandez for her advice and nice chats; to Sebastián Morales for his crazy stories; to Ángela Eslava for always giving me a good advice; to Fernanda Neira for being a source of encouragement; and to Maria Fernanda Limas for being a role model. Thanks to all of you for spending hours in your smartphones just for me.

Thanks for my former bosses, Ms. Eliana Lozano for her help and support; professor Francisco Boada for being my academic father back in Colombia; Mrs. Janneth

Sarmiento for believing in me, and Dr. Jairo Perilla for his knowledge, expertise, friendship, and help.

I must express my very profound gratitude to my brother Fabio Ruiz, and my parents, Fabio Ruiz Ramirez and Ana Marina Caldas for always being there, ready to support me at the distance. They always believed in me with such fervor that I was able to continue believing in myself when everything seemed to fall apart. Since I was a child, my parents instilled in me the value and power of education, they always said that I had the capacity to transform dreams into goals. Thanks to their hard work and dedication, I am here finishing one of my dreams. I am completely sure that this accomplishment would not have been possible without them. Thank you.

Finally, I will always be thankful for having the privilege to finish my engineering studies at the National University of Colombia. All my skills and expertise are due to my Alma Mater.

Table of Contents

List of Abbreviations

AGU	Anhydroglucosidic Unit
ATR	Attenuated Total Reflectance
BTEx	Benzene, Toluene, Ethylbenzene, And Xylene
cis-DCE	Cis-1,2-Dichloroethene
CMC	Carboxymethyl Cellulose
CNC	Cellulose Nanocrystal
CNF	Cellulose Nanofibril
DDT	Dichlorodiphenyltrichloroethane
DLS	Dynamic Light Scattering
DO	Deoxygenated
EDL	Electrical Double Layer
EDS	Energy Dispersive X-Ray Spectroscopy
EELS	Electron Energy Loss Spectroscopy
EtOH	Ethanol
FEG	Field Emission Gun
FeNP	Iron Nanoparticle
Fe-oxCNC	Iron - Carboxylated Cellulose Nanocrystal Nanocomposite
FTIR	Fourier-Transform Infrared Spectroscopy
GIF	Gatan Imaging Filtering
HCH	Hexachlorocyclohexane
ICP-OES	Inductively Coupled Plasma Optical Emission Spectrometry
ISCR	In-Situ Chemical Reduction
MMO	Metal, Metalloid, And Organometallic Compounds
NDMA	N-Nitrosodimethylamine
NOM	Natural Organic Matter
nZVI	Nanoscale Zero Valent Iron
oxCNC	Carboxylated Cellulose Nanocrystals
PAA	Poly(Acrylic Acid)
PAH	Polycyclic Aromatic Hydrocarbon
PCB	Polychlorinated Biphenyls
PHC	Petroleum Hydrocarbons
PMMA	Poly(Methyl Methacrylate)
PRB	Permeable Reactive Barriers

PSS	Poly-Styrene-Sulfonate
TCE	Trichloroethylene
TEM	Transmission Electron Microscopy
TEMPO	(2,2,6,6-Tetramethylpiperidin-1-Yl)Oxyl
TNT	Trinitrotoluene
TOC	Total Organic Carbon
ZVI	Zero Valent Iron

Preface

This work has been written in the following style for the efficient manuscript submission of chapters three (3) and four (4). This style implies some repetition between chapters concerning introduction and methodology. However, all results are unique. While receiving significant feedback and assistance in the performance of the research, I am the sole author of this work.

Chapter 1: Introduction

Over the past three decades, metallic iron, i.e. zerovalent iron (ZVI), has been found to be an effective agent to remediate a wide range of compounds including halogenated compounds[1][2][3], nitro aromatic compounds[4], nitrate compounds[5], and metallic ions[6][7]. Iron is a reducing agent of many redox-labile substances because Fe^0 is prone to oxidation, forming Fe^{2+} and subsequently further oxidizing to form Fe^{3+}. Moreover, iron is highly abundant [8] and the cheapest metal on earth [9]. As such, iron is cost-effective for soil and groundwater remediation [10].

A well-established method to increase iron remediation efficiency is to increase its surface area-to-volume ratio, achieved by reducing iron particle size. Iron nanoparticles can be highly reactive due to their large surface area to volume ratio [11]. *Wang et al.*[12] were the first to report a method of synthesizing nanoscale Zero-Valent Iron particles (nZVI), and report that these nanoparticles have higher reactivity rates than micron scale ZVI. Moreover, nZVI holds the potential of threat the same variety of pollutants as ZVI and its size would allow it to be injected in a broad range of locations.

Despite its many advantages, nZVI has several drawbacks limiting its practical applications, mainly its strong homo-aggregation [13]. nZVI is prone to homo-aggregation in part due to their strong attractive magnetic forces and low electrostatic repulsion[14][15]. As a result, nZVI has low soil mobility, limiting its ability to reach target contaminants in soils. Homo-aggregation also reduces its surface-area to volume advantages, limiting its reactivity towards contaminants in soils and groundwater. These issues significantly impact the practical use of nZVI for in-situ contaminant reduction.

Recently, alternatives have been proposed to overcome these limitations. One approach is the use of organic coatings to prevent nZVI homoaggregation. Synthetic

polymers such as poly-styrene-sulfonate (PSS)[14], poly(methyl methacrylate) (PMMA) [16], poly(acrylic acid) (PAA)[17], and Poly(N-vinyl-2-pyrrolidone)[18], and natural polymers such as starch[19][15], guar gum[15], carboxymethyl cellulose(CMC) [14][19][20] have been used for this purpose. However, coating nanoparticles passivates the reactive particle surface, reducing nanoparticle reactivity.

We predict that the use of rigid nanostructures would have a lower passivating effect as compared to large flexible macromolecules. Rigid nanostructures have been shown to be used as stabilizers in emulsions and suspensions such as carbon nanotubes[21][22] and silica nanoparticles with different morphologies [23][24][25].

Cellulose nanocrystals (CNCs) have potential as rigid stabilizers. Cellulose is the most abundant polymer on earth[21] and can be obtained from a wide variety of plants. When cellulose fibers are mechanically or chemically processed, two types of nanostructures can be obtained: cellulose nanocrystals (CNCs), and cellulose nanofibrils (CNFs). These two structures are bio sourced, non-toxic and relatively simple to purify.

Recently, there has been extensive research on CNCs due to their nanoscale dimensions, easy surface modification, abundant availability, and unique morphology[22][23]. The use of CNCs as support for metal nanoparticles have gained increasing attention due to the properties inherent to CNCs, such as its rod-like morphology, high surface area, and thermal and colloidal stability [24][22][23] in addition to their biodegradability and biocompatibility.

Various research groups have reported on the synthesis of metallic nanoparticles on raw CNCs by chemical and thermal reduction. Some of the metals deposited include copper [25], platinum [25], gold [25] [26], silver [25], nickel[27], selenium[28], palladium[29], iron and iron oxides [35][36][32].These syntheses often create long rods

sparsely covered in metals or individual spherical metallic nanoparticles adsorbed to the surface of CNCs.

Zhou et al. [33] used CNCs as morphology-inducing and coordinate agent for the synthesis of TiO_2 nanoparticles. They obtained uniform cube-shaped TiO_2 nanoparticles with high crystallinity only using $TiCl_4$ and CNCs as starting materials.

The large surface area and negative surface charge of CNCs suggest that a large number of nZVI nanoparticles might be stabilized in the presence of CNCs. Moreover, the presence of primary and secondary hydroxyl groups on the CNC surface enables additional chemical functionalization [22][34]. For example, the hydroxyl groups on the CNC surface can be converted into carboxyl groups using sodium hypochlorite (NaOCl) and the system (2,2,6,6-Tetramethylpiperidin-1-yl)oxyl-sodium bromide (TEMPO-NaBr) as catalyst[35]. Carboxyl groups can adsorb divalent metal ions by covalent binding[36][37] and can increase the density of nanoparticles deposit on the CNC surface[37]

Silver nanoparticles have primarily been deposited on TEMPO-oxidized CNCs (oxCNCs) [37][38][39], while metals such as copper[40] and gold[41] have been deposited on the surface of TEMPO-oxidized cellulose nanofibrils (CNFs), using carboxyl groups as anchor sites for the metallic nanoparticles.

This thesis focuses on the synthesis of iron nanoparticles mediated by cellulose nanocrystals. The synthesis, characterization, and optimization of nanocomposites composed of cellulose nanocrystals and iron using a classical redox reaction is presented. Our results highlight the impact of the surface charge, surface functional groups, and number of CNCs on the size, morphology, and stability of iron nanoparticles. This synthesis process can be extrapolated to other type of metals and

metal oxides, giving researchers an opportunity in controlling size and morphology of similarly redox-generated nanoparticles.

1.1 Thesis Outline

Chapter 1: Introduction. This chapter includes the introduction and gives an overview of the of the organization of the thesis.

Chapter 2: Literature review. This chapter summarizes a literature review and the fundamental principles related to this project. This chapter also includes the research objectives and references.

Chapter 3: "Nucleation, growth, and stability of Cellulose Nanocrystal-Stabilized Iron Nanoparticles". This chapter presents the synthesis of nZVI particles in the presence of CNCs. Our results highlight the influence of CNCs on the rates and mechanisms of nucleation, growth, aggregation, and aging of nZVI particles. Our work shows that CNCs act as effective stabilizers for preparing colloidally stable nZVI nanoparticles. These cellulose nanocrystal-stabilized nZVI nanoparticles demonstrate properties well-suited for enhanced soil and groundwater remediation. This manuscript is in preparation for publication.

Chapter 4: "One-step iron metallization of carboxylated cellulose nanocrystals". This chapter presents the synthesis of Iron nanoparticles (FeNPs) in the presence of carboxylated CNCs (oxCNCs). We analyze the influence of carboxylic groups on the final morphology adopted by FeNPs. oxCNCs also act as stabilizers but have a higher impact on the rates of nucleation and aggregation compared to raw CNCs. Carboxylated CNCs may be used as a template for other metal/metal oxide nanoparticles at ambient conditions without the use of additional chemicals. This manuscript is in preparation for publication.

Chapter 5: Conclusions. The final chapter explores main conclusions, major contributions and future work for this research project.

Chapter 2: Literature review

2.1 Soils: contamination and remediation

Environmental contamination represents a serious threat for marine and terrestrial ecosystems. It became a critical issue after the industrial revolution for the amount and variety of pollutants released to the environment [42]. According to Canada government, a contaminated site is *"one at which substances occur at concentrations (1) above background levels and pose or are likely to pose an immediate or long-term hazard to human health or the environment, or (2) exceeding levels specified in policies and regulations."* [43]

Soil contamination is a widespread problem in developed countries due to a long history of low or absent environmental protections. According to the European Environmental Agency, 340 000 contaminated sites in Europe have been identified, and there is an estimate of 2.5 million potentially contaminated sites around the continent[44].

Asian countries experience considerable contamination of agricultural soil and crops by trace elements. For example, it is estimated that about 20% of Chinese farmland is contaminated with Cd, Ni and As [45]

To date, there has been identified over 22 000 contaminated or suspected contaminated sites in urban, rural and remote areas across Canada, and approximately 3 800 of those sites are located in Ontario[43]. Most of the contaminants are normally concentrated in soils or soil-related media because soils are considered as the *ultimate sink* for contaminants that enter the environment [42], and contaminants tend to have longer residence times in soil than in water or air [46]. Soil contamination typically occurs in places where mainly industrial activities, inadequate waste disposal, and/or chemical spills have introduced excessive amounts of contaminants that cannot be

naturally degraded [44] (Figure 2.1). A common source of soil pollution in developing countries is the use of contaminated groundwater or wastewater for irrigation[45]. Additionally, some contaminants can be transported at large distances by the wind, rain, or groundwaters, and can pollute soils far from the release source[47].

Figure 2.1 Chromium contamination at abandoned chemical factory in Durres – Albania. At 2006, the area was contaminated with Lindane/ HCH and hexavalent chromium due to a former chemical plant [48]. *Left, change on vegetation in same area due to soil contaminants. Reprinted form United Nations Environment Programme Disasters and conflicts*[49]

In Canada, most frequent contaminants include metal, metalloid, and organometallic compounds(MMOs); petroleum hydrocarbons (PHCs); polycyclic aromatic hydrocarbon (PAHs); benzene, toluene, ethylbenzene, and xylene (BTEx); and Polychlorinated biphenyls (PCBs) [43]. The physical state of the contaminant varies depending on the type of contaminant and the type of soil. *Kabata et al.* [50] presents different interaction mechanisms between pollutants and soil particles (Figure 2.2). In general, the following forms can be observed:

- Particulate pollutants -with particle size over the same scale of soil particles-
- Liquid films around soil particles
- Pollutants adsorbed at the surface of soil particles
- Pollutants present as solids or liquids in the pores of soil particles

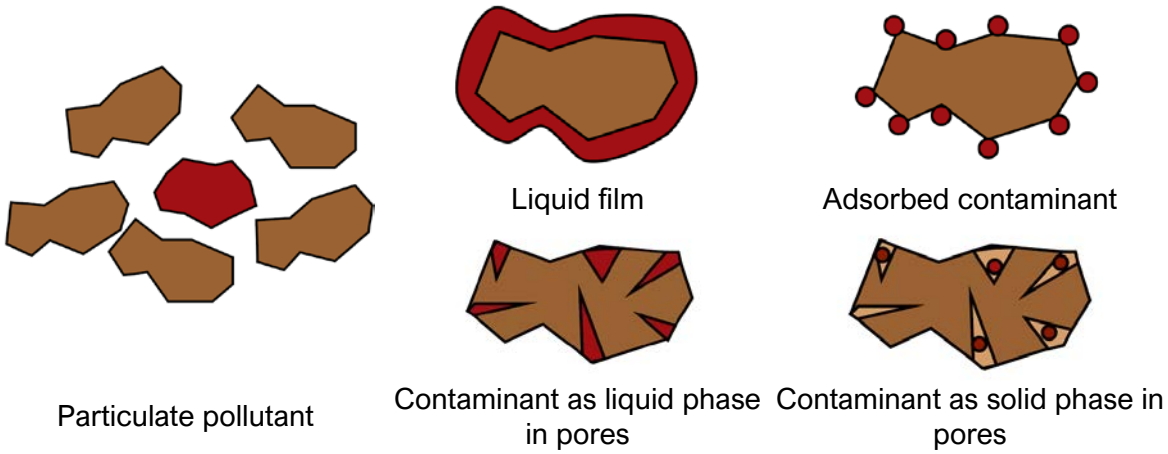

Figure 2.2 Physical state of contaminants in soils. Adapted from [50]

Soil contamination is an area of major concern due to its direct impact in agricultural production, natural environment and human health [47]. Soils are an essential constituent of the earth surface and play a vital role in life processes[51]. As a result of this situation, and the growing awareness and public concern about environmental contamination, soil remediation technologies have gained considerable importance in last decades [42][46].

Soil remediation represents a challenge due to the complexity and diversity of contaminants and sites where these contaminants are deposited. Conventional methods of soil remediation include: excavation and off-site disposal, soil flushing, incineration, vitrification, and capping [46]. The effective treatment of a contaminated soil depends on the proper selection, design, and implementation of a remediation technology. Two factors are key for the success of such technologies: to utilize low-impact materials and to be categorized as a cost-effective solution. Remediation costs varies significantly depending on the technology used. Ex-situ treatments include high costs associated with removal, transport and storage, while technologies such as incineration or vitrification also have high energy costs due to the high temperatures than must be

reached. Moreover, some technologies -such as capping and soil flushing- don't remove or transform the contaminant into a less toxic compound.

2.2 In situ chemical reduction and zero valent Iron (ZVI)

One of the most developed methods applied for in-situ soil remediation (i.e. without excavation nor transportation) is by chemical reduction. The main principle of in-situ chemical reduction (ISCR) is the addition of reducing agents to degrade pollutants into less toxic compounds [52]. The dehalogenation of chlorinated aliphatic or aromatic contaminants, and the reduction of nitroaromatic compounds [53] are some examples of chemical reductions involving organic pollutants. Some common reductants include reduced metal species such as Fe^{2+}, Fe_3O_4, and Fe^0, reduced sulfur species such as HS^-, $S_2O_4^{2-}$, FeS, FeS_2, and other electron-donating substances such as natural organic matter (NOM)[54]. The use of iron in its elemental state - Fe^0 or Zero-Valent Iron (ZVI)- is one of the most established technologies for treating contaminants [10][55] due to its intrinsic properties: Iron is highly abundant [8], the cheapest metal on earth [9], and it is prone to oxidation ($E° = -0.44V$). Moreover, iron oxyhydroxides can adsorb a variety of inorganic contaminants such as heavy metals and metalloids[56][57]. For example, from the most frequent contaminants in Canada, ZVI can treat MMOs and PCBs.

The earliest environmental use of ZVI was reported in 1982 by *Gould* [58] who studied the kinetics of reduction of hexavalent chromium -Cr (IV)- by metallic iron, while in 1994, *Gillham and O'Hannesin* [3] were the first to show the effectiveness of ZVI for reduce a variety of organic halogen compounds. Since the 90s, ZVI has been used in permeable reactive barriers (PRB) for the removal of chlorinated organic contaminants in-situ [55][59]

A permeable reactive barrier is a passive in-situ treatment zone that degrades or immobilizes contaminants as ground water flows through it [60].

The first pilot-scale PRB was installed in 1991 at Borden, Ontario, to treat chlorinated solvents, while the first full-scale commercial PRB was installed in 1994 at Sunnyvale, California, also for chlorinated solvents [61]. Since then, the use of PRBs has grown throughout the world. An example of the installation of a full-scale PRB is shown in Figure 2.3. This PRB consists of 3 segments of 1.2 m wide and 175 m long[62].

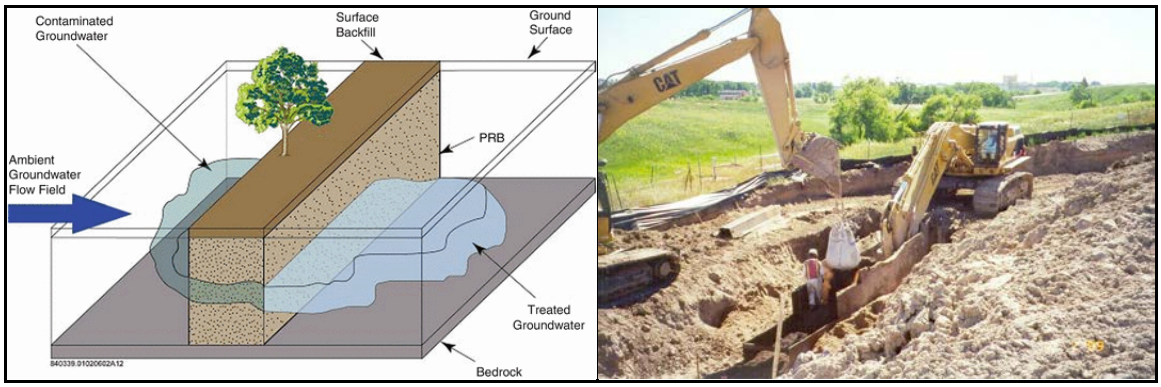

Figure 2.3 (Left) Layout of a permeable reactive barrier. As contaminated groundwater passes through the PRB, the reactive media inside remove or degrade the contaminants and the treated groundwater leaves the permeable reactive barrier. Reprinted from[63]. *(Right) Full scale PRB installed at F.E Warren Air Force Base, Cheyenne, WY for the treatment of chlorinated compounds (TCE and cis-DCE). Reprinted from*[62]

Concerning the mechanisms involved during contaminant reduction, *Matheson and Tratnyek* [2] proposed three different pathways for the reduction of halogenated compounds by ZVI (Figure 2.4): (a) reduction at the iron metal surface, (b) subsequent reduction by ferrous ions previously produced, and (c) reduction by generation and subsequent reaction with hydrogen if a catalyst is present.

In the case of inorganic contaminants, additional mechanisms have been proposed: reductive precipitation, surface adsorption or complexation, and coprecipitation with Fe oxyhydroxides formed on the ZVI surface(Figure 2.4-c,d) [10][64][65].

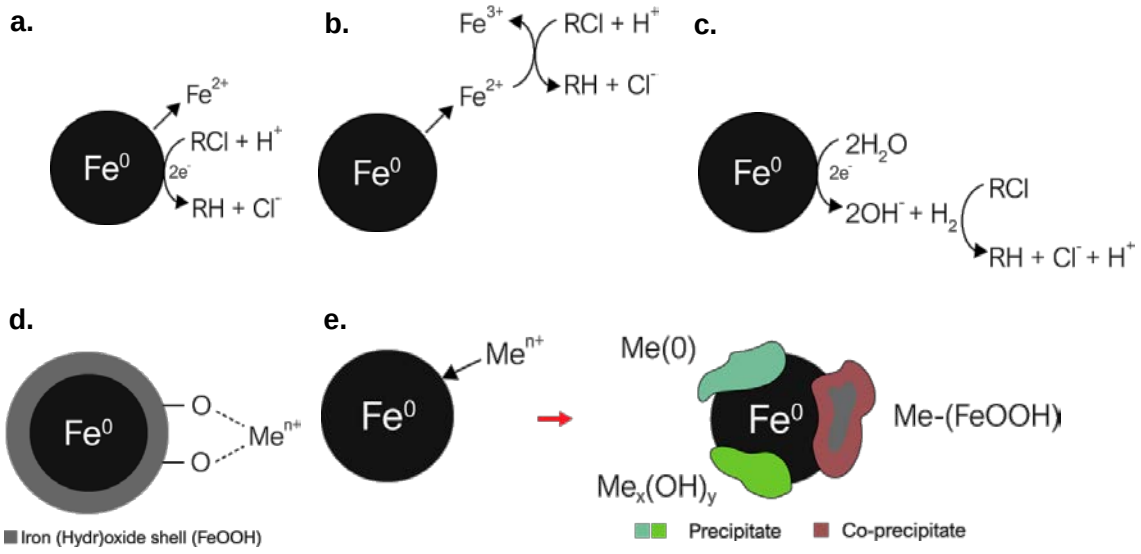

Figure 2.4 (Top) Reductive dehalogenation pathways by using zero-valent iron (ZVI): (a) Direct reduction at the metal surface. (b) Reduction by ferrous iron (c) hydrogenolysis by the hydrogen that is formed by the reduction of H2O during anaerobic corrosion. (Bottom) Mechanisms for the removal of inorganic compounds: (d) surface complexation (e) reductive precipitation and co-precipitation. Modified from [2][64]

2.3 Nano Zero Valent Iron (nZVI)

Although ZVI is an attractive material for environmental soil decontamination, important challenges still exist for the practical application of this technology. These limitations include: low reactivity due to the oxyhydroxide layer formed after iron corrosion, passivity of ZVI arising from certain contaminants and the need for large quantities of iron and high infrastructure costs for in-situ treatments[64] [66].

Some methods to overcome these disadvantages includes combinations of metallic iron and catalytic metals such as Pd or Ni, or the replacement of Fe^0 with more strongly reducing metals such as Zn^0[54].

Another popular approach in recent years has been the fabrication of nanoscale ZVI (nZVI). nZVI are iron nanoparticles with a core-shell structure comprised of a dense

metallic center (Fe^0) and an iron hydroxide shell, (mainly Fe_3O_4)[67]. nZVI possess a greater reactivity per mass of material, which significantly improves its remediation performance. Because of their size, nZVI has higher mobility through porous media, which would allow it to be injected in a broad range of locations. In 1997, *Wang et al.*[12] were the first researchers to report a method of synthesizing nZVI and show that these nanoparticles have higher reactivity rates than micro ZVI. Since then, nZVI has been intensively investigated as a new tool for soil remediation. Some topics studied in the last decades related to nZVI include comparisons between ZVI and nZVI, improvement of their mobility on porous media, bench scale and field applications, and environmental concerns related to these nanoparticles [55][68].

In 2001, the first field trial of the use of nZVI for the treatment of TCE in groundwater at a manufacturing site in Trenton, New Jersey, USA, was performed[69] At present time, nZVI particles are commercially available[70].

2.4 Removal of hazardous contaminants

Because the chemical composition of nZVI and ZVI is the same, nZVI holds the potential of threat the same pollutants as ZVI. After its first synthesis, the effectivity of nZVI in the removal/degradation of a wide range of chemical pollutants has been evaluated. *Wei-xian Zhang* [71] has compiled a wide range of contaminants that can be transformed using nZVI. Table 2-1 is an adaptation of his work and expanded to contain additional contaminants that have been shown to be treated by nZVI.

Chlorinated methanes	*Organic dyes*
Carbon tetrachloride (CCl_4)	Orange II ($C_{16}H_{11}N_2NaO_4S$)
Chloroform ($CHCl_3$)	Chrysoidine ($C_{12}H_{13}ClN_4$)
Dichloromethane (CH_2Cl_2)	Tropaeolin O ($C_{12}H_9N_2NaO_5S$)
Chloromethane (CH_3Cl)	Acid Orange
Chlorinated ethenes	Acid Red
Tetrachloroethene (C_2Cl_4)	*Pesticides*
Trichloroethene (C_2HCl_3)	DDT ($C_{14}H_9Cl_5$)
cis-Dichloroethene ($C_2H_2Cl_2$)	Lindane ($C_6H_6Cl_6$) [72]
trans-Dichloroethene ($C_2H_2Cl_2$)	*Other organic contaminants*
1,1-Dichloroethene ($C_2H_2Cl_2$)	N-nitrosodimethylamine (NDMA) ($C_4H_{10}N_2O$)
Vinyl chloride (C_2H_3Cl)	*Metal and metalloid ions*
Chlorinated benzenes	Mercury (Hg^{+})
Hexachlorobenzene (C_6Cl_6)[72]	Nickel (Ni^{2+})
Pentachlorobenzene (C_6HCl_5) [72]	Silver (Ag^{+})
Tetrachlorobenzenes ($C_6H_2Cl_4$)	Cadmium (Cd^{2+})
Trichlorobenzenes ($C_6H_3Cl_3$)	Arsenic (As^{5+},As^{3+})[7] [73]
Dichlorobenzenes ($C_6H_4Cl_2$)	Chromium (Cr^{6+})[73]
Chlorobenzene (C_6H_5Cl)	Barium (Ba^{6+})[73]
Other polychlorinated hydrocarbons	Cobalt (Co^{2+})[73]
PCBs	*Inorganic anions*
Dioxins	Dichromate ($Cr_2O_7^{2-}$)
Hexachlorobutadiene (C_4Cl_6) [72]	Arsenic (AsO_4^{3-})
Pentachlorophenol (C_6HCl_5O)	Perchlorate (ClO_4^{-})
Trihalomethanes	Nitrate (NO_3^{-})
Bromoform ($CHBr_3$)	*Radionuclides*
Dibromochloromethane ($CHBr_2Cl$)	Uranyl (UO_2^{2+})[74]
Dichlorobromomethane ($CHBrCl_2$)	
Nitroaromatic compounds	
TNT ($C_7H_5N_3O_6$)	
Nitrobenzene ($C_6H_5NO_2$)[75]	

Table 2-1 Common environmental contaminants that can be transformed by nZVI. Reprinted and modified from [71]

2.5 nZVI synthesis

To date, numerous methods have been developed for nZVI synthesis. In general, these methods can be classified in bottom-up and top-down methods . Some of the most important techniques are summarized below[41].

Thermal decomposition and electrolysis are the methods used at industrial scale while chemical reduction is more extended at the academic level[76].

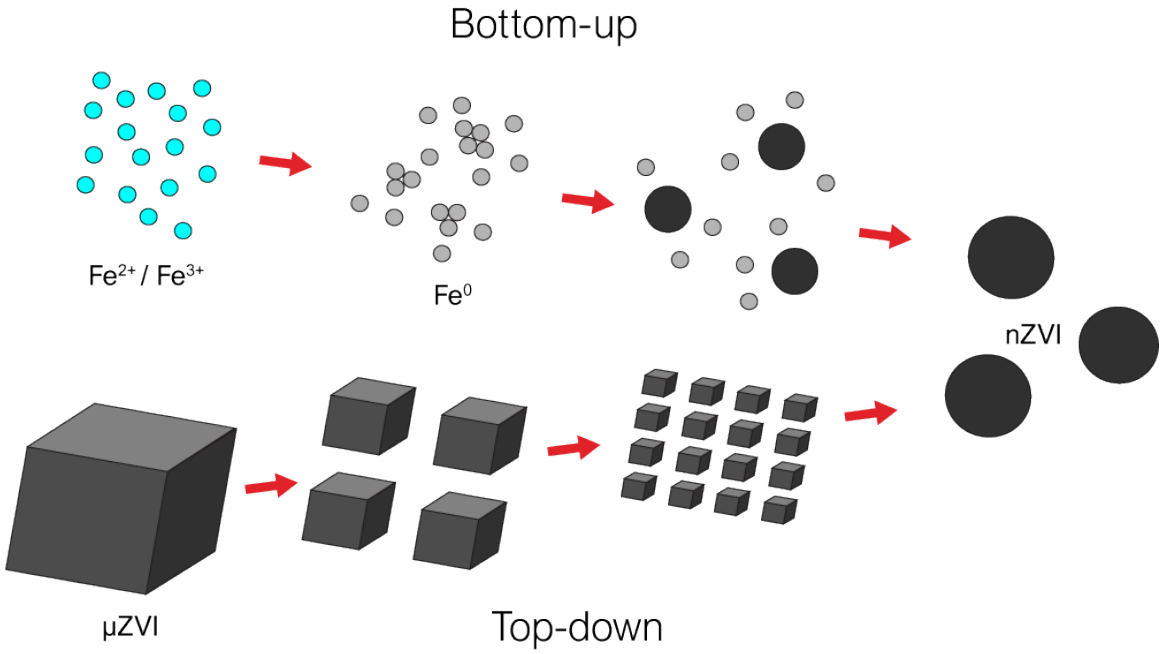

Figure 2.5 scheme of nanoparticles synthesis by top-down and bottom-up approaches for nZVI synthesis. Top-down methods include ball milling of bulk iron particles, while bottom-up methods include aqueous or thermal reduction of Fe^{2+} / Fe^{3+} ions or iron oxides. Modified from[77]

2.5.1 Chemical reduction

The first and the most popular method for the synthesis of nZVI particles is reducing metallic iron salts with a strong reducing agent. The first generation of nZVI particles were synthesized by reducing iron chloride with sodium borohydride [12]. Stochiometric amounts of sodium borohydride are slowly added at ambient temperature and inert atmosphere. The following reaction is involved:

$$Fe^{3+} + 3BH_4^- + 9H_2O \rightarrow Fe^0 + 3H_2BO_3^- + 12H^+ + 6H_2 \uparrow$$

$FeCl_3$ was replaced with $FeSO_4$ to reduce the amount of $NaBH_4$ required and the excessive amount of chloride in the final products. In this new process, the following reaction is involved:

$$Fe^{2+} + 2BH_4^- + 6H_2O \rightarrow Fe^0 + 2B(OH)_3 + 7H_2 \uparrow$$

The formation of metallic particles from a metallic salt takes the following steps: Formation of zero valent molecules through redox reduction, homogenous nucleation of zero valent molecules to form primary particles, growth of primary particles through molecular accretion, particle aggregation and/or coalescence to form secondary particles, and aggregation of secondary particles to form fractal aggregates [78]. The main disadvantages of this synthesis method are the toxicity and the high price of reducing agent[76]

2.5.2 Thermal decomposition

This method consists in the thermal reduction of iron oxides (e.g. FeOOH) or iron salts at high temperatures (>500°C) and using H_2 as reducing agents [79] Parameters such as the rate of heating, the temperature of reaction, and the annealing time have influence on the size and size distribution of the nanoparticles[80].

2.5.3 Electrolysis

This method produces nZVI particles from a solution with ferrous and/or ferric salts applying an electric current between an anode and a cathode. The synthesized nanoparticles are deposited on the cathode, and are further detached using ultrasonication or other methods[76]. This method is considered cheaper and faster than chemical reduction[76]. The only issue is the high aggregation of fresh metallic nanoparticles at the cathode[80].

2.5.4 Precision milling

It consists on crushing micro-sized ZVI particles using stainless steel beads in a high-speed rotary chamber[77]. This method is solvent-free and doesn't require sophisticated equipment. However, the nanoparticles produced have irregular shapes and have strong tendency to agglomerate[80]

2.5.5 Other techniques

nZVI has also been synthesized using chemical vapor deposition, vacuum evaporation and sputtering[79]. However, these techniques require larges amount of energy and sophisticated equipment. So, they have been limited to lab-scale research[77].

2.6 Main challenges in the use of nZVI particles

Despite its many advantages, nZVI particles have several obstacles to practical application, mainly due to their strong tendency to homoaggregate and adhere to solid surfaces[10][81]. As a result, nZVI has low soil mobility which limits its ability to reach target contaminants in soils. Different strategies have been developed to improve the colloidal stability of nZVI particles by lowering their interparticle attractions. These methods include metal doping, surface coating or nZVI deposition on supports[76]. Each method has its advantages and drawbacks.

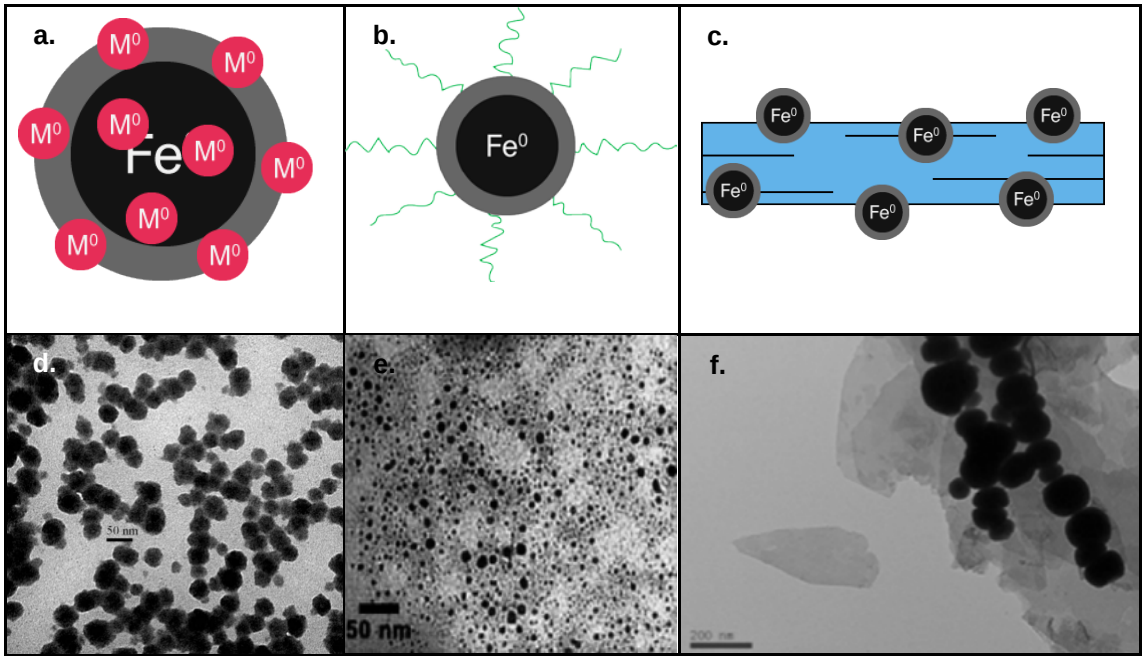

Figure 2.6. (Top) Scheme methods used for improving nZVI properties: (a) metal doping, (b) surface coating, and (c) nZVI deposition on supports. (Bottom) TEM Images of (d) nZVI and b Pd/Fe nanoparticles (Reprinted from[82]*), (e) CMC-coated nZVI (Reprinted from*[83]*), and (f) nZVI supported on zeolite (Reprinted from* [84]*).*

2.6.1 Metal doping

One method used to increase the effectiveness of nZVI is the coupling of nZVI with other metals to form a bimetallic nanoparticle. The doping metal acts a catalyst and increases the rate of reduction[85]. For example, In the case of Pd-nZVI particles, the increment on the rate of reduction is attributed to the galvanic contact between palladium and iron, which creates a large electrochemical potential difference[86], and the fact that palladium itself is a common catalyst for redox reactions.

Both effects result in enhanced iron corrosion. Some noble metals used to obtain bimetallic ZVI nanoparticles include Pd[82][87][88], Pt[88], Ag[89], Ni[88][90], and Cu[91].Palladium is the most common metallic catalyst used with nZVI for remediation purposes[76] .

The synthesis process consists in the reduction of a metal salt containing the doping metal:

$$Fe^0 + \frac{2}{n}M^{n+} \rightarrow Fe^{2+} + \frac{2}{n}M^0$$

The resulting nanoparticle has a layer of the doping metal on top of the nZVI surface [85]. At 2011, approximately 40% of all nZVI remediation projects in the US used bimetallic nZVI[92]

2.6.2 Supported nZVI

Solid materials such as silica [93][94], biochar[95][96], ionic resins[97][98], graphene [99][100][101], minerals such as bentonite[102], kaolin [103] and zeolite[84], and nanoporous networks made of covalent organic polymers[104] have been successfully tested as supporting materials. The use of solid supports reduces nZVI oxidation, controls aggregation and approaches the contaminant near the nZVI by adsorption to the support [76]

2.6.3 Surface coating

Coating the nZVI surface with a soluble polymer or surfactant increases the repulsive forces to overcome the magnetic and magnetic iron attractive forces[80]. These coatings also offer protection against iron oxidation.

Two approaches can be used for coating nanoparticles. One method involves mixing of coating solution with nZVI after particle synthesis (i.e., post-synthesis method), or the addition of a coating solution to the precursor solution of Fe prior to nZVI particle synthesis (i.e., pre-synthesis method). The pre-synthesis method yields nZVI suspensions with greater stability[83]

Synthetic polymers such as poly-styrene-sulfonate (PSS)[14], poly(methyl methacrylate) (PMMA) [16], poly(acrylic acid) (PAA)[17], and Poly(N-vinyl-2-

pyrrolidone)[18], natural polymers such as starch[19][15], guar gum[15], carboxymethyl cellulose(CMC) [14][19][20], and surfactants as Tween 85[105], SDS[106], and CTAB[106] have been used for this purpose.

Between these polymers, CMC have gained consideration over the last decade. CMC significantly improves the performance of nZVI particles[107]. Besides functioning as a stabilizer, CMC also provides an additional capacity for contaminant removal via adsorption[76]. For example, Wang et al. demonstrated that the Cr(VI) removal efficiency of CMC-stabilized nZVI is approximately four times higher than non-stabilized nZVI [49]. However, its main disadvantage is that CMC can generate complex with divalent cations present in soils, inducing precipitation and therefore reducing nZVI mobility in practical applications [108]

2.7 Cellulose nanocrystals

The colloidal stabilization of nZVI is essential for its practical use for soil remediation. One method to stop nZVI aggregation and improve nZVI mobility is the use of particle-stabilizing materials. We hypothesize that the use of a rigid structure will optimize the exposure of nZVI to contaminants, and a nanoscale stabilizer will have a smaller impact on nZVI mobility. A good support should also be nontoxic, environmentally friendly, low-cost, easily available, and stable against the changes that can occur in the sites in which nZVI is going to be used [76]

One nanoparticle that meet all these requirements are Cellulose nanocrystals. Cellulose nanocrystals (CNCs) are exceptional nanomaterials derived from cellulose, which is the most abundant biopolymer on earth[109] CNCs have been of great scientific interest due to their high crystallinity, low density, rod-like shape, high aspect ratio (diameter/length), high specific surface area, good mechanical properties (high stiffness and elastic modulus), low coefficient of thermal expansion, stability in

aggressive media, gas permeability and optical transparency[110]. Moreover, CNCs are biodegradable, sustainable, and highly abundant [111].

Various research groups have reported on the synthesis of metallic nanoparticles on raw CNCs by chemical and thermal reduction. Some of the metals deposited include copper [25], platinum [25], gold [26][25], silver [25], nickel[27], selenium[28], palladium[29], and iron[30], [31].These syntheses often create long rods sparsely covered in metals or individual spherical metallic nanoparticles adsorbed to the surface of CNCs.

The presence of primary and secondary hydroxyl groups on the CNC surface enables additional chemical functionalization [22][34]. For example, the hydroxyl groups on the CNC surface can be converted into carboxyl groups using sodium hypochlorite (NaOCl) and the system (2,2,6,6-Tetramethylpiperidin-1-yl)oxyl-sodium bromide (TEMPO-NaBr) as catalyst[35]. Carboxyl groups can adsorb divalent metal ions by covalent binding[36][37]. This surface functionality has been recently used to increase the density of nanoparticles deposit on the CNC surface[37]

Silver nanoparticles have primarily been deposited on TEMPO-oxidized CNCs [37][38][39], while metals such as copper[40] and gold[41] have been deposited on the surface of TEMPO-oxidized cellulose nanofibrils (CNFs), using carboxyl groups as anchor sites for the metallic nanoparticles.

2.8 Objectives

The goal of this research is to synthesize nanocomposites of nZVI loaded on cellulose nanocrystals. These nanoparticles will be synthesized by chemical reduction at ambient temperature without the use of additional chemicals or sophisticated equipment. Two nano cellulose-based supports with different surface functional groups will be used. We hypothesize that the number of supports in solution and the type of functional groups at the support surface will allow to tune the morphology of this

nanocomposite. We expect that improving the colloidal stability of nZVI through an environmentally friendly and biodegradable rigid support will enhance its potential for environmental applications. The specific objectives of this work include:

- To develop a cost-effective method to synthesize nanocomposites of iron supported on CNCs through chemical reduction. This method may be extrapolated to other metallic nanoparticles.
- To characterize the size distribution, morphology, colloidal stability, and chemical reactivity of the nanocomposites synthesized
- To study the effect of cellulose nanocrystals and oxidized cellulose nanocrystals on the mechanisms of nucleation, growth, aggregation and aging of iron nanoparticles.

2.9 References

[1] R. W. Gillham and S. F. O'Hannesin, "Enhanced Degradation of Halogenated Aliphatics by Zero-Valent Iron," *Groundwater*, vol. 32, no. 6, pp. 958–967, Nov. 1994.

[2] L. J. Matheson and P. G. Tratnyek, "Reductive Dehalogenation of Chlorinated Methanes by Iron Metal," *Environ. Sci. Technol.*, vol. 28, no. 12, pp. 2045–2053, 1994.

[3] S. F. O'Hannesin and R. W. Gillham, "Long-Term Performance of an In Situ "Iron Wall" for Remediation of VOCs," *Ground Water*, vol. 36, no. 1, pp. 164–170, Jan. 1998.

[4] A. Agrawal and P. G. Tratnyek, "Reduction of nitro aromatic compounds by zero-valent iron metal," *Environ. Sci. Technol.*, vol. 30, no. 1, pp. 153–160, Jan. 1996.

[5] C.-P. Huang, H.-W. Wang, and P.-C. Chiu, "Nitrate reduction by metallic iron," *Water Res.*, vol. 32, no. 8, pp. 2257–2264, 1998.

[6] K. J. Cantrell, D. I. Kaplan, and T. W. Wietsma, "Zero-valent iron for the in situ remediation of selected metals in groundwater," *J. Hazard. Mater.*, vol. 42, no. 2, pp. 201–212, Jul. 1995.

[7] N. P. Nikolaidis, G. M. Dobbs, and J. A. Lackovic, "Arsenic removal by zero-valent iron: Field, laboratory and modeling studies," *Water Res.*, vol. 37, no. 6, pp. 1417–1425, Mar. 2003.

[8] I. McDonald *et al.*, "Rusty old stars: A source of the missing interstellar iron?," *Astrophys. J. Lett.*, vol. 717, no. 2 PART 2, pp. L92–L97, Jul. 2010.

[9] J. Emsley, *The Elements*, 3rd editio. Oxford Chemistry Guides, 1998.

[10] F. Fu, D. D. Dionysiou, and H. Liu, "The use of zero-valent iron for groundwater remediation and wastewater treatment: A review," *J. Hazard. Mater.*, vol. 267, pp. 194–205, 2014.

[11] M. Otto, M. Floyd, and S. Bajpai, "Nanotechnology for site remediation," *Remediat. J.*, vol. 19, no. 1, pp. 99–108, 2008.

[12] W.-X. Zhang and C.-B. Wang, "Rapid and complete dechlorination of TCE and PCBs by nanoscale Fe and Pd/Fe particles," vol. 37, No. 1, no. 7, pp. 78–79, 1997.

[13] H.-J. Lu, J.-K. Wang, S. Ferguson, T. Wang, Y. Bao, and H. Hao, "Mechanism, synthesis and modification of nano zerovalent iron in water treatment," *Nanoscale*, vol. 8, no. 19, pp. 9962–9975, 2016.

[14] T. Phenrat, N. Saleh, K. Sirk, H. J. Kim, R. D. Tilton, and G. V. Lowry, "Stabilization of aqueous nanoscale zerovalent iron dispersions by anionic polyelectrolytes: Adsorbed anionic polyelectrolyte layer properties and their effect on aggregation and sedimentation," *J. Nanoparticle Res.*, vol. 10, no. 5, pp. 795–814, 2008.

[15] A. Tiraferri, K. L. Chen, R. Sethi, and M. Elimelech, "Reduced aggregation and sedimentation of zero-valent iron nanoparticles in the presence of guar gum," *J. Colloid Interface Sci.*, vol. 324, no. 1–2, pp. 71–79, 2008.

[16] W. Wang, M. Zhou, Z. Jin, and T. Li, "Reactivity characteristics of poly(methyl methacrylate) coated nanoscale iron particles for trichloroethylene remediation," *J. Hazard. Mater.*, vol. 173, no. 1–3, pp. 724–730, Jan. 2010.

[17] Y. H. Lin, H. H. Tseng, M. Y. Wey, and M. Der Lin, "Characteristics of two types of stabilized nano zero-valent iron and transport in porous media," *Sci. Total Environ.*, vol. 408, no. 10, pp. 2260–2267, 2010.

[18] Y. Xu, X. Zhang, Y. Hsing, and Y. Fang, "Ultrasonic-assisted Synthesis of Fe Nanoparticles in the Presence of Poly (N-vinyl-2-pyrrolidone)," *Chinese J. Chem.*, vol. 29, no. 9, pp. 1829–1836, 2011.

[19] Q. Liang, D. Zhao, T. Qian, K. Freeland, and Y. Feng, "Effects of Stabilizers and Water Chemistry on Arsenate Sorption by Polysaccharide-Stabilized Magnetite Nanoparticles," *Ind. Eng. Chem. Res.*, vol. 51, no. 5, pp. 2407–2418, Feb. 2012.

[20] R. L. Johnson *et al.*, "Field-Scale Transport and Transformation of Carboxymethylcellulose-Stabilized Nano Zero-Valent Iron," *Environ. Sci. Technol.*, vol. 47, no. 3, pp. 1573–1580, 2013.

[21] S. Kalia *et al.*, "Cellulose-based bio- and nanocomposites: A review," *Int. J. Polym. Sci.*, vol. 2011, 2011.

[22] R. J. Moon, A. Martini, J. Nairn, J. Simonsen, and J. Youngblood, "Cellulose nanomaterials review: Structure, properties and nanocomposites," *Chemical Society Reviews*, vol. 40, no. 7. pp. 3941–3994, 2011.

[23] H. Liu, J. Song, S. Shang, Z. Song, and D. Wang, "Cellulose nanocrystal/silver nanoparticle composites as bifunctional nanofillers within waterborne polyurethane," *ACS Appl. Mater. Interfaces*, vol. 4, no. 5, pp. 2413–2419, 2012.

[24] M. Kaushik and A. Moores, "Review: Nanocelluloses as versatile supports for metal nanoparticles and their applications in catalysis," *Green Chemistry*, vol. 18, no. 3. pp. 622–637, 2016.

[25] S. Padalkar *et al.*, "Natural biopolymers: Novel templates for the synthesis of nanostructures," *Langmuir*, vol. 26, no. 11, pp. 8497–8502, 2010.

[26] Y. Shin, I. T. Bae, B. W. Arey, and G. J. Exarhos, "Facile stabilization of gold-silver

alloy nanoparticles on cellulose nanocrystal," *J. Phys. Chem. C*, vol. 112, no. 13, pp. 4844–4848, 2008.

[27] Y. Shin, I. T. Bae, B. W. Arey, and G. J. Exarhos, "Simple preparation and stabilization of nickel nanocrystals on cellulose nanocrystal," *Mater. Lett.*, vol. 61, no. 14–15, pp. 3215–3217, Jun. 2007.

[28] Y. Shin, J. M. Blackwood, I. T. Bae, B. W. Arey, and G. J. Exarhos, "Synthesis and stabilization of selenium nanoparticles on cellulose nanocrystal," *Mater. Lett.*, vol. 61, no. 21, pp. 4297–4300, Aug. 2007.

[29] M. Rezayat, R. K. Blundell, J. E. Camp, D. A. Walsh, and W. Thielemans, "Green One-Step Synthesis of Catalytically Active Palladium Nanoparticles Supported on Cellulose Nanocrystals," 2014.

[30] P. Dhar, A. Kumar, and V. Katiyar, "Fabrication of cellulose nanocrystal supported stable Fe(0) nanoparticles: a sustainable catalyst for dye reduction, organic conversion and chemo-magnetic propulsion," *Cellulose*, vol. 22, no. 6, pp. 3755–3771, Dec. 2015.

[31] N. Bossa, A. W. Carpenter, N. Kumar, C.-F. de Lannoy, and M. Wiesner, "Cellulose nanocrystal zero-valent iron nanocomposites for groundwater remediation," *Environ. Sci. Nano*, vol. 4, no. 6, pp. 1294–1303, 2017.

[32] K. K. Sadasivuni, D. Ponnamma, H.-U. Ko, H. C. Kim, L. Zhai, and J. Kim, "Flexible NO 2 sensors from renewable cellulose nanocrystals/iron oxide composites," *Sensors Actuators B. Chem.*, vol. 233, pp. 633–638, 2016.

[33] Y. Zhou, E. Y. Ding, and W. D. Li, "Synthesis of TiO2 nanocubes induced by cellulose nanocrystal (CNC) at low temperature," *Mater. Lett.*, vol. 61, no. 28, pp. 5050–5052, 2007.

[34] S. Eyley and W. Thielemans, "Surface modification of cellulose nanocrystals," *Nanoscale*, vol. 6, no. 14, pp. 7764–7779, 2014.

[35] Y. Habibi, H. Chanzy, and M. R. Vignon, "TEMPO-mediated surface oxidation of cellulose whiskers," *Cellulose*, vol. 13, no. 6, pp. 679–687, 2006.

[36] R. K. Cannan and A. Kibrick, "Complex Formation between Carboxylic Acids and Divalent Metal Cations," *J. Am. Chem. Soc.*, vol. 60, no. 10, pp. 2314–2320, Oct. 1938.

[37] N. Meulendijks *et al.*, "Electrically conductive coatings consisting of Ag-decorated cellulose nanocrystals," *Cellulose*, vol. 24, no. 5, pp. 2191–2204, 2017.

[38] H. Liu, D. Wang, Z. Song, and S. Shang, "Preparation of silver nanoparticles on cellulose nanocrystals and the application in electrochemical detection of DNA hybridization," *Cellulose*, vol. 18, no. 1, pp. 67–74, 2011.

[39] K. M. A. Uddin, A. R. Lokanathan, A. Liljeström, X. Chen, O. J. Rojas, and J. Laine, "Silver nanoparticle synthesis mediated by carboxylated cellulose nanocrystals," *Green Mater.*, vol. 2, no. 4, pp. 183–192, 2014.

[40] R. Bendi and T. Imae, "Renewable catalyst with Cu nanoparticles embedded into cellulose nano-fiber film," *RSC Adv.*, vol. 3, no. 37, pp. 16279–16282, 2013.

[41] A. Azetsu, H. Koga, A. Isogai, and T. Kitaoka, "Synthesis and Catalytic Features of Hybrid Metal Nanoparticles Supported on Cellulose Nanofibers," *Catalysts*, vol. 1, no. 1, pp. 83–96, Nov. 2011.

[42] H. Meuser, *Soil Remediation and Rehabilitation*, vol. 23. 2013.

[43] T. B. of C. Secretariat, "Federal Contaminated Sites Inventory," 2018. [Online]. Available: http://www.tbs-sct.gc.ca/fcsi-rscf/home-accueil-eng.aspx. [Accessed:

27-Aug-2018].

[44] European Commission, "Soil Contamination : Impacts on Human Health," *Sci. Environ. Policy*, no. 5, pp. 1–29, 2013.

[45] FAO and ITPS, *Status of the World's Soil Resources (SWSR) - Main Report.* 2015.

[46] E. Lombi and R. E. Hamon, "REMEDIATION OF POLLUTED SOILS," in *Encyclopedia of Soils in the Environment*, Elsevier, 2005, pp. 379–385.

[47] M. K. Hill, *Understanding Environmental Pollution*. 2010.

[48] M. Mansaku-Meksi, B. Baraj, E. Center, and R. A. Frashëri, "International POPs Elimination Project Fostering Active and Efficient Civil Society Participation in Preparation for Implementation of the Stockholm Convention Country Situation Report on Persistent Organic Pollutants in Bangladesh Environment and Social," 2005.

[49] United Nations Environment Programme Disasters & Conflicts Sub-Programme, "Albania," 2000. [Online]. Available: https://www.flickr.com/photos/unep_dc/with/8901030188/. [Accessed: 04-Sep-2018].

[50] A. Kabata-Pendias, *Heavy Metals*. Berlin, Heidelberg: Springer Berlin Heidelberg, 1995.

[51] B. Dedieu and G. Serviere, *Twenty years of research and development on work in livestock farming: achievements and prospects*, vol. 25, no. 2. 2012.

[52] R. D. Fox, "Physical/chemical treatment of organically contaminated soils and sediments," *Journal of the Air and Waste Management Association*, vol. 46, no. 5. pp. 391–413, 20-May-1996.

[53] P. Tratnyek and D. Macalady, "Oxidation-Reduction Reactions in the Aquatic Environment," in *Handbook of Property Estimation Methods for Chemicals*, CRC Press, 2000.

[54] P. G. Tratnyek, R. L. Johnson, G. V Lowry, and R. A. Brown, "IN SITU Chemical Reduction For Source Remediation," in *Chlorinated Solvent Source Zone Remediation*, B. H. Kueper, H. F. Stroo, C. M. Vogel, and C. H. Ward, Eds. New York, NY: Springer New York, 2014, pp. 307–351.

[55] M. I. Litter, *Iron Nanomaterials for Water and Soil Treatment*. 2018.

[56] B. KA, "Case studies for immobilizing toxic metals with iron coprecipitation and adsorption.," in *Env. Separation of Heavy Metals*, vol. 26, 2001, pp. 181–204.

[57] R. R. Gadde and H. A. Laitinen, "Studies of Heavy Metal Adsorption by Hydrous Iron and Manganese Oxides," *Anal. Chem.*, vol. 46, no. 13, pp. 2022–2026, Nov. 1974.

[58] J. P. Gould, "The kinetics of hexavalent chromium reduction by metallic iron," *Water Res.*, vol. 16, no. 6, pp. 871–877, 1982.

[59] G. A. Boshoff and B. Bone, *Permeable Reactive Barriers*. Wallingford International Association of Hydrological Sciences, 2005.

[60] US EPA, "Field Applications of In Situ Remediation Technologies: Permeable Reactive Barriers," *USEPA Publ.*, vol. EPA 542-R-, pp. 1–122, 1999.

[61] K. Bronstein, "Permeable Reactive Barriers for Inorganic and Radionuclide," 2005.

[62] Remediation Technologies Development Forum (RTDF), "Profile PRB F.E. Warren Air Force Base, Cheyenne, WY." [Online]. Available: https://rtdf.clu-

in.org/public/permbarr/PRBSUMMS/profile.cfm?mid=81. [Accessed: 04-Sep-2018].

[63] V. Asokbunyarat, P. N. L. Lens, and A. P. Annachhatre, "Permeable Reactive Barriers for Heavy Metal Removal," 2017, pp. 65–100.

[64] X. Q. Li, D. W. Elliott, and W. X. Zhang, "Zero-valent iron nanoparticles for abatement of environmental pollutants: Materials and engineering aspects," *Crit. Rev. Solid State Mater. Sci.*, vol. 31, no. 4, pp. 111–122, 2006.

[65] C. L. Geiger, K. Carvalho-Knighton, S. Novaes-Card, P. Maloney, and R. DeVor, "A Review of Environmental Applications of Nanoscale and Microscale Reactive Metal Particles," pp. 1–20, 2010.

[66] X. Guan *et al.*, "The limitations of applying zero-valent iron technology in contaminants sequestration and the corresponding countermeasures: The development in zero-valent iron technology in the last two decades (1994–2014)," *Water Res.*, vol. 75, pp. 224–248, May 2015.

[67] A. Liu, J. Liu, and W. xian Zhang, "Transformation and composition evolution of nanoscale zero valent iron (nZVI) synthesized by borohydride reduction in static water," *Chemosphere*, vol. 119, pp. 1068–1074, 2015.

[68] X. Zhao, W. Liu, Z. Cai, B. Han, T. Qian, and D. Zhao, "An overview of preparation and applications of stabilized zero-valent iron nanoparticles for soil and groundwater remediation," *Water Res.*, vol. 100, pp. 245–266, 2016.

[69] D. W. Elliott and W. Zhang, "Field Assessment of Nanoscale Bimetallic Particles for Groundwater Treatment," *Environ. Sci. Technol.*, vol. 35, no. 24, pp. 4922–4926, Dec. 2001.

[70] NANO IRON future technology, "NANOFER STAR SDS," 2017. [Online]. Available: http://nanoiron.cz/getattachment/81874e2a-f96f-455e-8551-14f40f67868c/NANOFER-STAR-SDS-English.aspx. [Accessed: 04-Sep-2018].

[71] W. X. Zhang, "Nanoscale iron particles for environmental remediation: An overview," *J. Nanoparticle Res.*, vol. 5, no. 3–4, pp. 323–332, 2003.

[72] K. Šimkovič, J. Derco, and M. Valičková, "Removal of selected pesticides by nano zero-valent iron," *Acta Chim. Slovaca*, vol. 8, no. 2, pp. 152–155, 2015.

[73] K. T. Soto-Hidalgo and C. R. Cabrera, "Nanoscale Zero Valent Iron for Environmental Cadmium Metal Treatment," in *Green Chemistry*, H. E.-D. M. Saleh and M. Koller, Eds. Rijeka: IntechOpen, 2018.

[74] O. Riba, T. B. Scott, K. Vala Ragnarsdottir, and G. C. Allen, "Reaction mechanism of uranyl in the presence of zero-valent iron nanoparticles," *Geochim. Cosmochim. Acta*, vol. 72, no. 16, pp. 4047–4057, 2008.

[75] M. Tong, S. Yuan, H. Long, M. Zheng, L. Wang, and J. Chen, "Reduction of nitrobenzene in groundwater by iron nanoparticles immobilized in PEG/nylon membrane," *J. Contam. Hydrol.*, vol. 122, no. 1–4, pp. 16–25, 2011.

[76] M. Quaiserrsaquibb, A. Alatarr, and A. Al-Khedhairy Editors, *Phytotoxicity of Nanoparticles*. Cham: Springer International Publishing, 2018.

[77] S. Li, W. Yan, and W. X. Zhang, "Solvent-free production of nanoscale zero-valent iron (nZVI) with precision milling," *Green Chem.*, vol. 11, no. 10, pp. 1618–1626, 2009.

[78] N. T. K. Thanh, N. Maclean, and S. Mahiddine, "Mechanisms of nucleation and growth of nanoparticles in solution," *Chemical Reviews*. 2014.

[79] M. Kumar and G. Chann, *Nanocomposites in Wastewater Treatment*. 2015.

[80] J. Adusei-Gyamfi and V. Acha, "Carriers for nano zerovalent iron (nZVI): synthesis, application and efficiency," *RSC Adv.*, vol. 6, no. 93, pp. 91025–91044, 2016.

[81] R. Mukherjee, R. Kumar, A. Sinha, Y. Lama, and A. K. Saha, "A review on synthesis, characterization, and applications of nano zero valent iron (nZVI) for environmental remediation," *Critical Reviews in Environmental Science and Technology*, vol. 46, no. 5. pp. 443–466, 2016.

[82] X. Chen *et al.*, "Hydrodechlorination of polychlorinated biphenyls in contaminated soil from an e-waste recycling area, using nanoscale zerovalent iron and Pd/Fe bimetallic nanoparticles," *Environ. Sci. Pollut. Res.*, vol. 21, no. 7, pp. 5201–5210, 2014.

[83] F. He and D. Zhao, "Manipulating the size and dispersibility of zerovalent iron nanoparticles by use of carboxymethyl cellulose stabilizers," *Environ. Sci. Technol.*, vol. 41, no. 17, pp. 6216–6221, 2007.

[84] S. A. Kim *et al.*, "Removal of Pb(II) from aqueous solution by a zeolite-nanoscale zero-valent iron composite," *Chem. Eng. J.*, vol. 217, pp. 54–60, 2013.

[85] D. O'Carroll, B. Sleep, M. Krol, H. Boparai, and C. Kocur, "Nanoscale zero valent iron and bimetallic particles for contaminated site remediation," *Adv. Water Resour.*, vol. 51, pp. 104–122, 2013.

[86] W. Yan, A. A. Herzing, X. Q. Li, C. J. Kiely, and W. X. Zhang, "Structural evolution of Pd-doped nanoscale zero-valent iron (nZVI) in aqueous media and implications for particle aging and reactivity," *Environ. Sci. Technol.*, vol. 44, no. 11, pp. 4288–4294, 2010.

[87] C.-B. Wang and W. Zhang, "Synthesizing Nanoscale Iron Particles for Rapid and Complete Dechlorination of TCE and PCBs," *Environ. Sci. Technol.*, vol. 31, no. 7, pp. 2154–2156, Jul. 1997.

[88] W. X. Zhang, C. B. Wang, and H. L. Lien, "Treatment of chlorinated organic contaminants with nanoscale bimetallic particles," *Catal. Today*, vol. 40, no. 4, pp. 387–395, 1998.

[89] Y. Xu and W. X. Zhang, "Subcolloidal Fe/Ag particles for reductive dehalogenation of chlorinated benzenes," *Ind. Eng. Chem. Res.*, vol. 39, no. 7, pp. 2238–2244, 2000.

[90] A. D. Bokare, R. C. Chikate, C. V Rode, and K. M. Paknikar, "Iron-nickel bimetallic nanoparticles for reductive degradation of azo dye Orange G in aqueous solution," *Appl. Catal. B Environ.*, vol. 79, no. 3, pp. 270–278, 2008.

[91] D. Sparis, C. Mystrioti, A. Xenidis, and N. Papassiopi, "Reduction of nitrate by copper-coated ZVI nanoparticles," *Desalin. Water Treat.*, vol. 51, no. 13–15, pp. 2926–2933, Mar. 2013.

[92] R. A. Crane and T. B. Scott, "Nanoscale zero-valent iron: Future prospects for an emerging water treatment technology," *J. Hazard. Mater.*, vol. 211–212, no. 212, pp. 112–125, 2011.

[93] E. Petala *et al.*, "Nanoscale zero-valent iron supported on mesoporous silica: Characterization and reactivity for Cr(VI) removal from aqueous solution," *J. Hazard. Mater.*, vol. 261, pp. 295–306, 2013.

[94] X. Qiu, Z. Fang, B. Liang, F. Gu, and Z. Xu, "Degradation of decabromodiphenyl ether by nano zero-valent iron immobilized in mesoporous silica microspheres," *J. Hazard. Mater.*, vol. 193, pp. 70–81, 2011.

[95] H. Dong *et al.*, "Stabilization of nanoscale zero-valent iron (nZVI) with modified biochar for Cr(VI) removal from aqueous solution," *J. Hazard. Mater.*, vol. 332, pp. 79–86, 2017.

[96] X. Peng *et al.*, "New insights into the activity of a biochar supported nanoscale zerovalent iron composite and nanoscale zero valent iron under anaerobic or aerobic conditions," *RSC Adv.*, vol. 7, no. 15, pp. 8755–8761, 2017.

[97] A. Toli, K. Chalastara, C. Mystrioti, A. Xenidis, and N. Papassiopi, "Incorporation of zero valent iron nanoparticles in the matrix of cationic resin beads for the remediation of Cr(VI) contaminated waters," *Environ. Pollut.*, vol. 214, pp. 419–429, 2016.

[98] H. Park, Y.-M. Park, K.-M. Yoo, and S.-H. Lee, "Reduction of nitrate by resin-supported nanoscale zero-valent iron," *Water Sci. Technol.*, vol. 59, no. 11, pp. 2153–2157, Jun. 2009.

[99] H. Chen, Y. Cao, E. Wei, T. Gong, and Q. Xian, "Facile synthesis of graphene nano zero-valent iron composites and their efficient removal of trichloronitromethane from drinking water," *Chemosphere*, vol. 146, pp. 32–39, 2016.

[100] Z. J. Li *et al.*, "Efficient removal of uranium from aqueous solution by zero-valent iron nanoparticle and its graphene composite," *J. Hazard. Mater.*, vol. 290, pp. 26–33, 2015.

[101] X. Lv *et al.*, "Nanoscale Zero-Valent Iron (nZVI) assembled on magnetic Fe3O4/graphene for Chromium (VI) removal from aqueous solution," *J. Colloid Interface Sci.*, vol. 417, pp. 51–59, 2014.

[102] Z.-X. Chen, X.-Y. Jin, Z. Chen, M. Megharaj, and R. Naidu, "Removal of methyl orange from aqueous solution using bentonite-supported nanoscale zero-valent

iron," *J. Colloid Interface Sci.*, vol. 363, pp. 601–607, 2011.

[103] Z.-X. Chen, Y. Cheng, Z. Chen, M. Megharaj, and R. Naidu, "Kaolin-supported nanoscale zero-valent iron for removing cationic dye-crystal violet in aqueous solution."

[104] P. D. Mines, J. Byun, Y. Hwang, H. A. Patel, H. R. Andersen, and C. T. Yavuz, "Nanoporous networks as effective stabilisation matrices for nanoscale zero-valent iron and groundwater pollutant removal," *J. Mater. Chem. A*, vol. 4, no. 2, pp. 632–639, 2015.

[105] A. K. Ibrahem, T. Abdel Moghny, Y. M. Mustafa, N. E. Maysour, F. Mohamed Saad El Din El Dars, and R. Farouk Hassan, "Degradation of Trichloroethylene Contaminated Soil by Zero-Valent Iron Nanoparticles," *ISRN Soil Sci.*, vol. 2012, pp. 1–9, 2012.

[106] S. Chatterjee, S.-R. Lim, and S. H. Woo, "Removal of Reactive Black 5 by zero-valent iron modified with various surfactants," *Chem. Eng. J.*, vol. 160, pp. 27–32, 2010.

[107] Q. Wang, H. Qian, Y. Yang, Z. Zhang, C. Naman, and X. Xu, "Reduction of hexavalent chromium by carboxymethyl cellulose-stabilized zero-valent iron nanoparticles," *J. Contam. Hydrol.*, vol. 114, pp. 35–42, 2010.

[108] R. Singh and V. Misra, "Stabilization of Zero-Valent Iron Nanoparticles: Role of Polymers and Surfactants," in *Handbook of Nanoparticles*, Cham: Springer International Publishing, 2015, pp. 1–18.

[109] Y. Habibi, L. A. Lucia, and O. J. Rojas, "Cellulose nanocrystals: Chemistry, self-assembly, and applications," *Chem. Rev.*, vol. 110, no. 6, pp. 3479–3500, 2010.

[110] D. García-García, R. Balart, J. Lopez-Martinez, M. Ek, and R. Moriana, "Optimizing the yield and physico-chemical properties of pine cone cellulose nanocrystals by different hydrolysis time," *Cellulose*, vol. 25, no. 5, pp. 2925–2938, 2018.

[111] L. Brinchi, F. Cotana, E. Fortunati, and J. M. Kenny, "Production of nanocrystalline cellulose from lignocellulosic biomass: Technology and applications," *Carbohydrate Polymers*, vol. 94, no. 1. pp. 154–169, 2013.

[112] T. Phenrat, N. Saleh, K. Sirk, R. D. Tilton, and G. V. Lowry, "Aggregation and sedimentation of aqueous nanoscale zerovalent iron dispersions," *Environ. Sci. Technol.*, vol. 41, no. 1, pp. 284–290, 2007.

[113] M. S. Reid, M. Villalobos, and E. D. Cranston, "Benchmarking Cellulose Nanocrystals: From the Laboratory to Industrial Production," *Langmuir*, vol. 25, 2017.

[114] F. He and D. Zhao, "Manipulating the size and dispersibility of zerovalent iron nanoparticles by use of carboxymethyl cellulose stabilizers," *Environ. Sci. Technol.*, vol. 41, no. 17, pp. 6216–6221, 2007.

[115] I. V Markov, *Crystal Growth for Beginners*. WORLD SCIENTIFIC, 2003.

[116] P. H. Haumesser, *Nucleation and Growth of Metals: From Thin Films to Nanoparticles*. Elsevier Ltd, 2016.

[117] S. Kudera, L. Carbone, L. Manna, and W. J. Parak, "Growth mechanism, shape and composition control of semiconductor nanocrystals," in *Semiconductor Nanocrystal Quantum Dots: Synthesis, Assembly, Spectroscopy and Applications*, A. L. Rogach, Ed. Vienna: Springer Vienna, 2008, pp. 1–34.

[118] Q. Wu *et al.*, "Rheological behavior of cellulose nanocrystal suspension: Influence of concentration and aspect ratio," *J. Appl. Polym. Sci.*, vol. 131, no. 15, p. n/a-n/a, Aug. 2014.

[119] S. Wilson and L. F. Greenlee, "Post-Synthesis Separation and Storage of Zero-Valent Iron Nanoparticles," *J. Nanosci. Nanotechnol.*, vol. 17, no. 4, pp. 2413–2422, Apr. 2017.

[120] E. J. Reardon, "Anaerobic Corrosion of Granular Iron: Measurement and Interpretation of Hydrogen Evolution Rates," *Environ. Sci. Technol.*, vol. 29, no. 12, pp. 2936–2945, Dec. 1995.

[121] J. A. (John A. Blackman, "Metallic Nanoparticles," Elsevier Science, 2008, p. iii.

[122] L. Nicolais and G. Carotenuto, *Nanocomposites*. Hoboken, NJ: John Wiley & Sons, Inc, 2013.

[123] M. M. Khattab, N. A. Abdel-Hady, and Y. Dahman, "Cellulose nanocomposites," in *Cellulose-Reinforced Nanofibre Composites*, Elsevier, 2017, pp. 483–516.

[124] S. Montanari, M. Roumani, L. Heux, and M. R. Vignon, "Topochemistry of carboxylated cellulose nanocrystals resulting from TEMPO-mediated oxidation," *Macromolecules*, vol. 38, no. 5, pp. 1665–1671, 2005.

[125] D. da Silva Perez, S. Montanari, and M. R. Vignon, "TEMPO-mediated oxidation of cellulose III," *Biomacromolecules*, vol. 4, no. 5, pp. 1417–1425, 2003.

[126] M. Xu, H. Dai, X. Sun, S. Wang, and W. Wu, "Influence of buffer solution on tempo-mediated oxidation," *BioResources*, vol. 7, no. 2, pp. 1633–1642, 2012.

[127] P. J. Wyatt, "Measurement of Special Nanoparticle Structures by Light Scattering," 2014.

[128] F. Cherhal, F. Cousin, and I. Capron, "Influence of charge density and ionic strength on the aggregation process of cellulose nanocrystals in aqueous suspension, as revealed by small-angle neutron scattering," *Langmuir*, vol. 31, no. 20, pp. 5596–5602, 2015.

[129] A. J. Bard, L. R. Faulkner, N. York, C. @bullet, W. Brisbane, and S. E. Toronto, *ELECTROCHEMICAL METHODS Fundamentals and Applications*. 1944.

[130] J. D. Hem, F. A. Seaton, and T. B. Nolan, "Complexes of Ferrous Iron with Tannic Acid Chemistry of iron in natural water."

[131] I. M. Kolthoff, "Conductometric Titrations," *Ind. Eng. Chem. - Anal. Ed.*, vol. 2, no. 3, pp. 225–230, 1930.

[132] S. Machado *et al.*, "Application of green zero-valent iron nanoparticles to the remediation of soils contaminated with ibuprofen," *Sci. Total Environ.*, vol. 461–462, pp. 323–329, 2013.

Chapter 3: Nucleation, growth, and stability of Cellulose Nanocrystal-Stabilized Iron Nanoparticles

Abstract: Colloidally-stable zero valent iron nanoparticles (nZVI) were synthesized through a classical redox reaction of iron sulfate with minor modifications using cellulose nanocrystals (CNCs) as stabilizers. We obtained spherical nZVI particles with high surface roughness and a mean size of 130nm. Particles remain colloidally stable after more than two months. Cellulose nanocrystals play a dual role in nZVI stability: a foreign surface to encourage stable nucleation over fast aggregation and a stabilizer to prevent iron nanoparticles aggregating into fractal colloids. Our results highlight the impact of the presence of CNCs on the rates and mechanisms of nucleation, growth, aggregation, and aging of nZVI particles, indicating promise in controlling size and morphology of similarly redox-generated nanoparticles. Cellulose nanocrystal-stabilized nZVI nanoparticles demonstrate properties well-suited for enhanced soil and groundwater remediation.

3.1 Introduction

In last two decades, Nanoscale zero-valent iron particles (nZVI) have emerged as a promising material for in-situ soil remediation because of its high surface area to volume ratio, high reactivity, and versatility for the treatment of a wide variety of organic and inorganic compounds [Chapter 2]. However, nZVI is prone to rapid homoaggregation mainly due to its high attractive forces among particles[112], which limits their mobility in porous media.

One approach to overcome this disadvantage and improve the colloidal stability of nZVI dispersions, is the use of organic coatings as steric stabilizers. Synthetic polymers such as poly-styrene-sulfonate (PSS)[14], poly(methyl methacrylate) (PMMA) [16], poly (acrylic acid) (PAA)[17], and Poly(N-vinyl-2-pyrrolidone)[18], and natural polymers such as starch[19][15], guar gum[15], carboxymethyl cellulose(CMC) [14][19][20] have been used for this purpose. Although the stability of nZVI can be enhanced by surface coatings, coating nanoparticles passivates the reactive particle surface, reducing nanoparticle reactivity. We hypothesized that the use of nano-sized rigid stabilizers would have a lower passivating effect as compared to large flexible macromolecules.

Bossa et al. [31] showed that cellulose nanocrystals (CNCs) are one possible rigid support for nZVI. However, their work has several gaps concerning the influence of CNCs in the final morphology adopted by nZVI and its mechanism of aging. Cellulose is the most prevalent natural polymer, and CNCs are its rod-like naturally occurring crystalline nanostructure, which has been intensely studied in recent years[4].

Previous works reported the synthesis of metallic nanoparticles on raw CNCs by chemical and thermal reduction. Some of the metals deposited include copper [25], platinum [25], gold [25][26], silver [25], nickel[27], selenium[28], palladium[29], iron and iron oxides [30], [31] [32].

In this work, we synthesized CNC-supported nZVI nanoparticles with highly controlled growth and purification conditions leading to nanoparticles with enhanced properties for soil and groundwater remediation.

Moreover, the mechanism for nZVI nanoparticle evolution from nucleation to aging has been investigated. The size, morphology, and stability of nZVI nanoparticles has been found to be regulated by varying the CNC concentration in the reaction medium. We analyzed the synthesized particles using Transmission Electron Microscopy (TEM) and Energy Dispersive X-ray Spectroscopy (EDS), while the particle stabilization was monitored visually and quantified using Inductively Coupled Plasma Optical Emission Spectrometry (ICP-OES). Finally, the influence on CNCs in the rates and mechanisms of nucleation, growth, and aging was explored.

3.2 Materials and methods

3.2.1 Materials

Cellulose nanocrystals (CNCs) with 0-2% sulfur content were purchased from the University of Maine as ~98% freeze-dried powder. Nitrogen (>99.999%) was obtained from Air Liquide. The following chemicals were used as received: Iron(II) sulfate heptahydrate ($FeSO_4 \cdot 7H_2O$, ≥98.0%, Sigma Aldrich), sodium borohydride ($NaBH_4$ 98%, Alfa Aesar), and ethanol (94.0% - 96.0% ACS - BDH - VWR international). Ultrapure water (18.2 MΩ) was used throughout the study.

3.2.2 Synthesis of nanostructures.

Stabilized nZVI nanoparticles were prepared by modifying the conventional borohydride reduction method [12] through the addition of CNC nanoparticles.

In all experiments, the mass of iron was kept constant and only the amount of CNCs was modified to obtain the desired CNC: Fe2+ ratio. For this work, three molar ratios were tested: 1:1, 4:1 and 8:1. This ratio refers to the moles of anhydroglucosidic units

(AGU) found on the CNCs per mol of iron. For example, an 8:1 ratio of moles of AGU found on CNCs per moles of iron, (CNC: Fe2+), corresponds to 110.7 mg of CNCs for 10 mg of Fe (see Table 3-1).

A 25mg/mL stock solution of CNC was used for all the sets of experiments. This solution was prepared dispersing freeze dried CNCs using an ultrasonic homogenizer (500 W, 20 kHz, Q500, Qsonica) at 40% of amplitude with an on/off pulse of 2 s for 5min. Previously made CNC solutions were separately purged of oxygen by bubbling N_2 gas for at least 15 min right before use.

DI water was heated above 70°C for at least 30 min and then purged sparging 99% N_2 gas for the same time to produce deoxygenated (DO) water. All the solutions added during the synthesis process were prepared using deoxygenated (DO) water.

The synthesis was carried out in a 50 mL round bottom flask with a constant flow of N_2 gas. Bubbling N_2 also aided in mixing the solution in the absence of magnetic stirring. First, the required amount of solution of CNCs was added to the bottom flask and diluted using DO water to get a total volume of 44mL. A fresh solution of $FeSO_4$ was prepared immediately before iron reduction. 49.8 mg $FeSO_4 \cdot 7H_2O$ (corresponding to 10mg of Iron) were dissolved in 1mL of DO water and were added to the CNC solution.

A summary of the volumes and concentrations used in the synthesis process is shown in Table 3-1.

The CNC-$FeSO_4$ aqueous mixture was sparged with N_2 for at least 15 min to encourage mixing and ensure that Fe^{2+} diffused to the negatively charged sites on the CNC surface. nZVI particles were formed near negatively charged sites of the CNC by reducing Fe^{2+} ions using 5 mL of a borohydride solution (introduced at a rate of 500µL/min) in a BH_4^-/Fe^{2+} molar ratio of 2:1. A 10% excess of borohydride was used to ensure total reduction to nZVI since some borohydride is also consumed in reaction

with water. After completing the borohydride addition, the flask was left for at least 30 minutes to ensure complete iron reduction. In all the experiments, the final concentration of iron was 0.2g/L. The nanocomposite solution was stored in ambient conditions without further treatment.

For further comparison, raw nZVI (i.e., without CNCs in solution) was also synthesized following the procedure previously described.

System	CNC nZVI 1:1	CNC nZVI 4:1	CNC nZVI 8:1	Raw nZVI
Molar ratio (CNC:Fe)	1:1	4:1	8:1	-
Molar ratio (-SO_3H:Fe)	1:19.3	1:4.8	1:2.4	-
Mass ratio (CNC:Fe)	2.77:1	11.07:1	22.13:1	-
Mass CNC added (mg)	27.7	110.7	221.4	-
Concentration CNC (wt. %)	0.055%	0.221%	0.443%	-
Mass $FeSO_4 \cdot 7H_2O$ added (mg)	49.8	49.8	49.8	49.8
Equivalent mass Fe added (mg)	10	10	10	10
Mass $NaBH_4$ added	15.2	15.2	15.2	15.2

Table 3-1. Summary CNC:nZVI synthesis experimental parameter values. The parameter Molar ratio (-SO_3H:Fe) was calculated using the sulfate half-ester content of 335 mmol/kg of CNC reported by Reid et al[113] *for this same type of CNCs.*

The synthesis process of CNC-supported nZVI particles (CNC:nZVI) is illustrated in Scheme 3.1

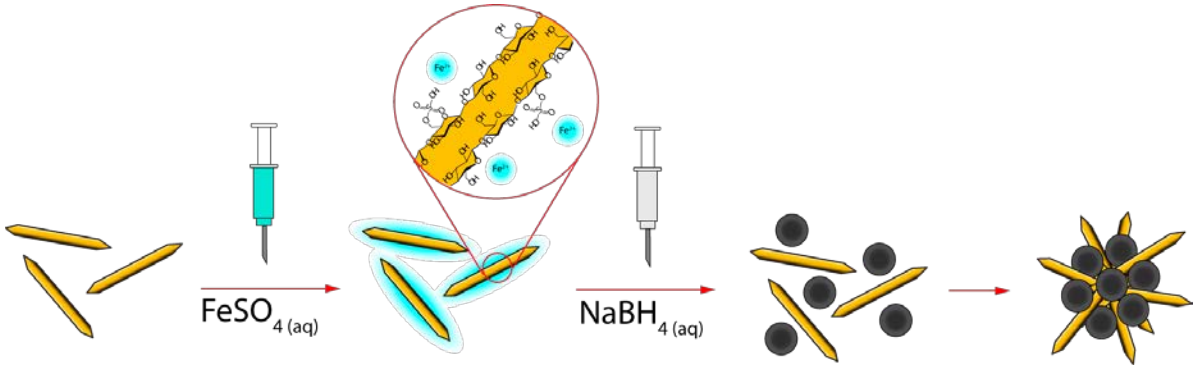

Scheme 3.1. Illustration of CNC:nZVI synthesis. The rod-like particles represent cellulose nanocrystals (CNC) while the black core-shell spheres represent metallic iron nanoparticles. A typical example of these nanoclusters is shown in Figure 3.2.

3.2.3 Nanostructure characterization

3.2.3.1 Colloidal stability

10mL of fresh nanoparticle suspensions (either raw nZVI or CNC:nZVI) were transferred into 10mL vials and kept under lab conditions (22°C, atmospheric pressure), to track their stability over time. The vials were monitored by visual inspection for 20 days, and the changes were recorded by photographs.

4mL of fresh CNC:nZVI were added in a glass vial and were allowed to settle for 20 days under ambient conditions. The amount of colloidally stable iron in solution was measured using Inductively Coupled Plasma-Optical Emission Spectrometer (Varian Vista Pro ICP-OES) and compared with the total amount of iron added to the vial initially. The iron content was measured at wavelengths of 234.350nm, 238.204nm, 258.588nm, and 259.940nm comparing it with the working standard solutions which were prepared by diluting a multielement standard solution (Sigma Aldrich) on HNO_3 10% w/v. A total of five (5) standard solutions were prepared: 100ppb, 500ppb, 1ppm, 5ppm, 10ppm. The samples were diluted 10-fold or 50-fold in HNO_3 10% w/v (See Table S3-1). Due to their much larger particle size, raw nZVI was first dissolved in HCl 35%

and then diluted 50-fold in HNO_3. Three (3) samples were analyzed for each batch of CNC:nZVI

3.2.3.2 Size, morphology, mechanism of formation and aging

TEM was used to evaluate the size and morphology of the CNC:nZVI nanoparticles. The measurements were performed on a Philips CM12 microscope operated at 120 kV. An amount of freshly prepared samples of CNC:nZVI nanoparticles were diluted to get a concentration of 100ppm of analytes (CNC and nZVI) before analysis. Two different solvents were used to make the dilutions: a solution of ethanol 60% v/v and DO water.

The ethanol-diluted samples were sonicated in an ultrasonic bath for 30 s. A drop (5 µL, 100 mg/mL in either 60%EtOH or DO water) of the CNC:nZVI diluted solution was placed on a holey carbon-coated copper grid.

The drop was allowed to dry on the grid for at least one hour. At least 100 particles were measured to evaluate the particle morphology and size distribution. ImageJ v1.52a software was used to analyze the TEM images. Two histograms were generated: one corresponding to the particle size distribution with bin sizes of 20 nm and a second of surface roughness with bin sizes of 0.1.

The water-dissolved samples were prepared in the same way as the ethanol-dissolved samples. At least 500 particles were measured to evaluate the size distribution of smaller particles observed in water-dissolved samples. Two particle size distribution histograms were generated, a particle-number normalized and a particle-volume normalized with a bin size of 25nm each.

The electron microscopy studies were performed in a JEOL 2010F equipped with a field emission gun (FEG) operated at 200kV. The composition of CNC : nZVI

nanoparticles was investigated by EDS analysis using an Oxford Inca EDS system. The grids previously prepared for the TEM images were used for this analysis.

3.3 Results

Figure 3.1a. shows zero-valent iron nanoparticles synthesized without support (raw nZVI) and with CNCs at different CNC:nZVI ratios of 1:1, 4:1, and 8:1. After less than 1h without mixing, the particles without support (raw nZVI) precipitate, while the CNC-supported nZVI particles remain colloidally stable. From Figure 3.1a, it is clear that CNCs prevent nZVI homo-aggregation. Within one day in these sealed vials, there is no noticeable difference between the particles synthesized with different amounts of support. However, the raw nZVI become fully oxidized, evident from their change in color from black to orange in less than one day (Figure 3.1b). The oxidation of CNC-supported nZVI only occurs after several days. The ratio of CNC to nZVI has an observable impact on the nanoparticle aging rate, suggesting a difference in aging mechanism among these solutions (Figure 3.1c).

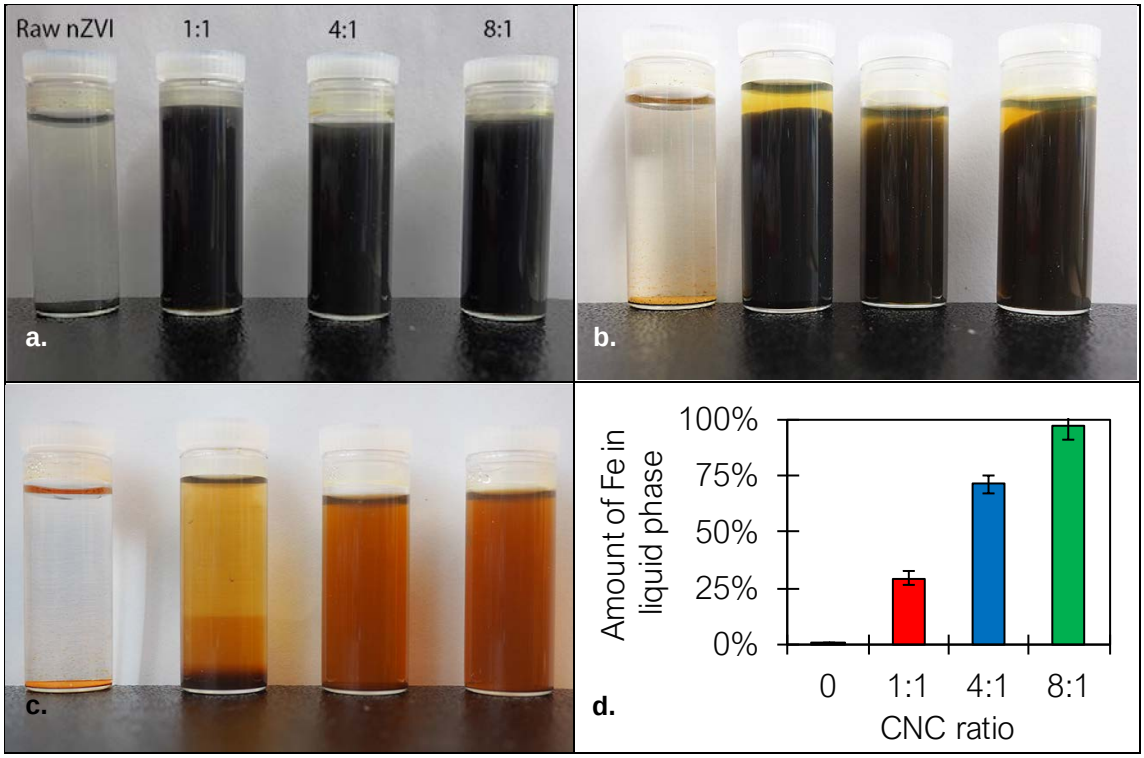

Figure 3.1. Photographs of (a) fresh, (b) 1-day aged, (c) and 40-day aged iron nanoparticles with different amounts of CNC as support (From left to right: Bare nZVI -, CNC:nZVI A - CNC:nZVI B - CNC:nZVI C). CNCs-supported iron particles are colloidally stable. (d) ICP-OES measurements showing the amount of colloidally stable nZVI with respect to the ratio of CNC added. Error bars are the standard deviation.

To determine the fraction of the nZVI that aggregates, we quantify the fraction of iron sedimented within the vials through ICP-OES measurements. Figure 3.1d shows the percentage of colloidally stable iron compared with the total amount of iron inside each vial. As can be seen, there is a dependence on the amount of colloidally stable nZVI with the amount of CNCs added to the system.

We used TEM to analyze the impact of CNCs on the change in Fe^0 nanoparticle (nZVI) morphology. Figure 3.2 shows how nZVI morphology and rugosity (i.e., surface roughness) changes with different amounts of CNCs added to the reaction media before redox reactions occur. These TEM images are reproducible and representative of at least 100 particles across duplicate samples. These samples were diluted using Ethanol

60% v/v as solvent. Particles synthesized without the presence of CNCs formed chain-like aggregates whose length were on the order of micrometers (Figure 3.2a). In contrast, nZVI particles synthesized using CNCs as support mainly form ~130nm spherical aggregate particles made from ~20nm *primary* particles, as can be seen in Figure 3.2. The mean size of spherical aggregates is consistent with previous studies [31] and similar morphologies were reported by Cheng et al[9] on iron-oxide nanoparticles synthesized at high temperatures using polyols as solvents. To our knowledge, this is the first reported observation of such primary particles synthesized in aqueous conditions at ambient temperature. Aggregated *primary* particles create nanometer scale roughness over the surface of the ~130nm spherical aggregate particles.

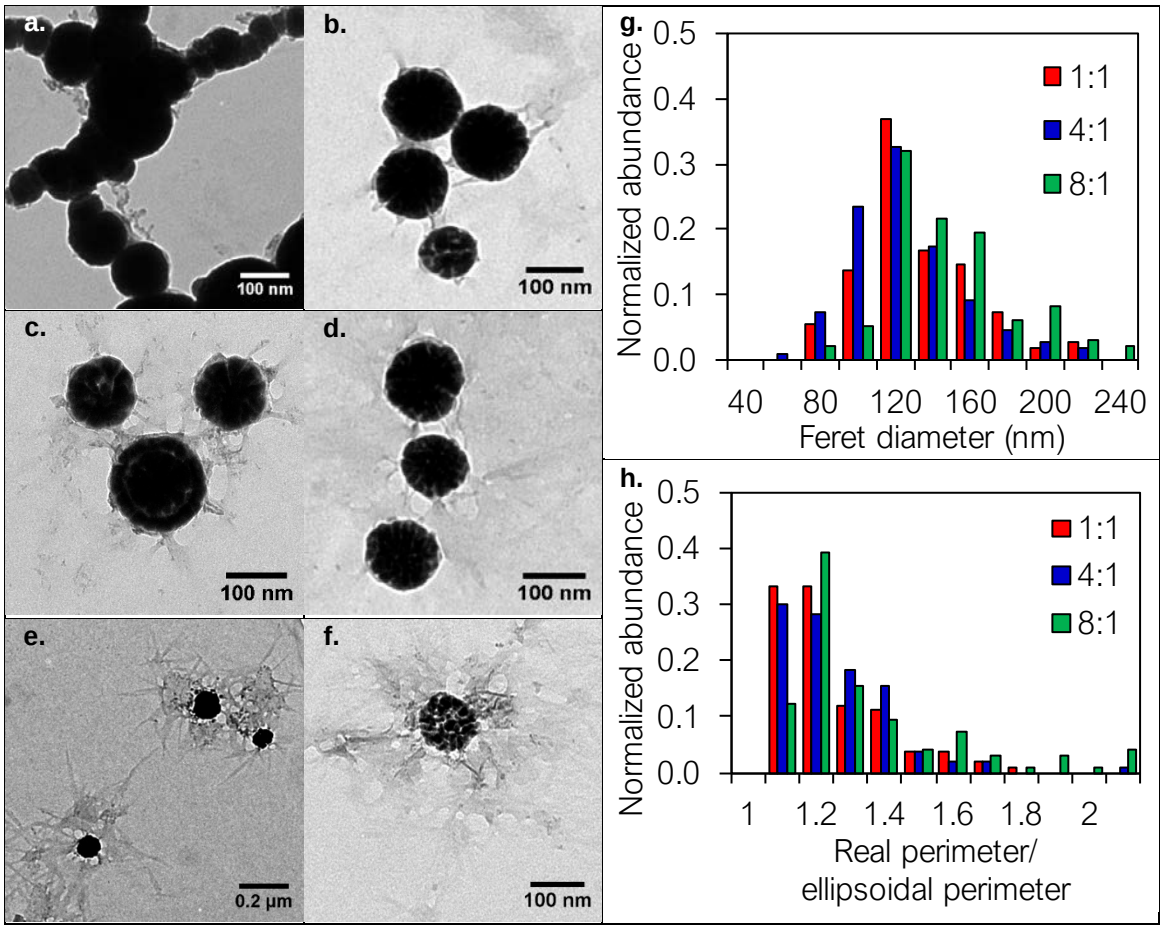

Figure 3.2. (a-d) TEM images of iron particles with different amounts of CNC as support. Bare nZVI (a) CNC:nZVI 11(b) CNC:nZVI 41(c) CNC:nZVI 81 (d). CNCs have a strong

influence on the size and morphology of the particles. (e) lower magnification TEM image of iron nanoparticles surrounded by CNCs for the system CNC:nZVI ratio of 8:1. The brightness and contrast of the image were modified to improve the visibility of the CNC nanoparticles . (f) A secondary particle (d~130nm) is made from aggregates of primary particles (d~20 nm) and surrounded by CNCs. A similar orientation of CNCs to nZVI was observed for the other evaluated ratios All the samples were diluted in ethanol 60% v/v. (g) Particle size distribution and (h) circularity distribution histograms of nZVI particles

The corresponding particle size distribution and rugosity of the obtained nanoparticles are given in Figure 3.2. We use the Feret diameter (F_d) – Defined as the maximum distance between two tangents on opposite sides of a particle – to quantify particle size in Figure 3.2g. For the roughness, we use the ratio between the perimeter of the particle obtained on ImageJ and the ellipsoidal perimeter (Eq. 1).

$$R_{np} = \frac{\sqrt{2}P}{\pi\sqrt{F_d^2 + f_d^2}} \qquad \textit{Eq. 1.}$$

R_{np}: Roughness nanoparticle

F_d: Feret diameter

f_d: minimum Feret diameter

P: Perimeter

The amount of CNCs added does not have a statistically relevant impact on the mean size or sphericity of the nZVI particles, however greater amounts of CNCs produce a broader distribution of sizes and non-spherical particles, with 8:1 ratio producing prominent number of aggregates above 180 nm and circularity ratios > 1.6 as compared with lower CNC ratios.

Each nZVI particle can be seen to be surrounded by several CNC particles, as observed in the TEM images (Figure 3.2). At high magnification, the cellulose nanocrystals cannot be easily differentiated from the carbon present on the TEM

copper grid, due to the low contrast resulting from carbon dominating the composition of cellulose[25]. However, at lower magnification, it is possible to see the cellulose nanocrystals surrounding nanoparticles of iron (Figure 3.2).

TEM samples were also prepared using water as solvent to encourage rapid aging (Figure 3.3c, d). These samples were compared with the TEM images obtained using ethanol 60% v/v (Figure 3.3 a, b). A 60%v/v solution of ethanol was used instead of pure ethanol to avoid CNC or nZVI homoaggregation while preventing oxidation. Fewer spherical aggregates, the presence of many small nanoparticles (< 20 nm) and nanocrystalline iron oxide were observed in the water-diluted samples as compared to the ethanol-diluted samples. All particles in ethanol are secondary nZVI particles adsorbed to CNCs, as shown in the TEM images of Figure 3.3a,b. nZVI in DO water, however, were observed to have substantially fewer secondary particles, as demonstrated in the TEM images in Figure 3.3c and an unexpectedly high number of primary particles (Figure 3.3c,d). All of the primary nanoparticles are attached to the CNCs (Figure 3.3d). The iron composition of the primary nanoparticles was confirmed using EDS; Figure 3.4), which shows that these particles are composed of iron and have a higher oxygen content than ethanol-dissolved samples.

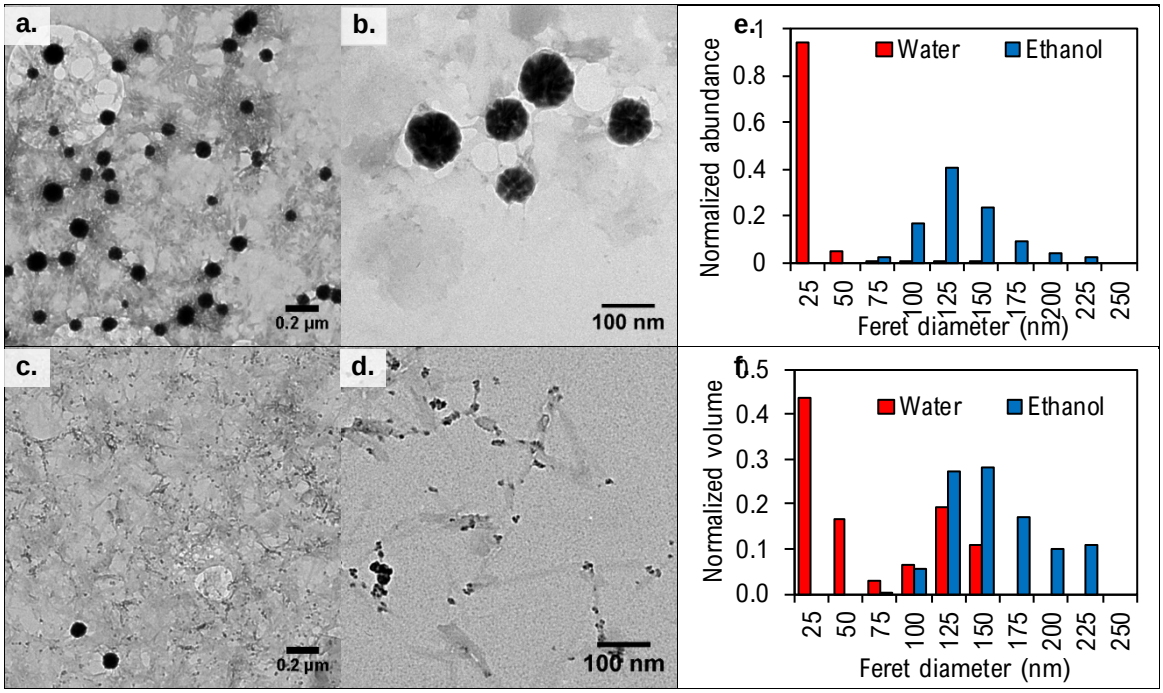

Figure 3.3. (a-d) TEM images of CNC-nZVI nanocomposites dissolved in 60% EtOH (top) and dissolved in water (bottom) during grid preparation. Secondary particles have the same size and morphology in both water and ethanol, but a burst of smaller particles is only seen in water-dissolved samples. (e) Number-weighted and (f) volume-weighted histogram size distribution of particles dissolved in water and ethanol. A bimodal distribution can be observed in the water-dissolved samples. All data correspond to the ratio CNC to nZVI 1:1

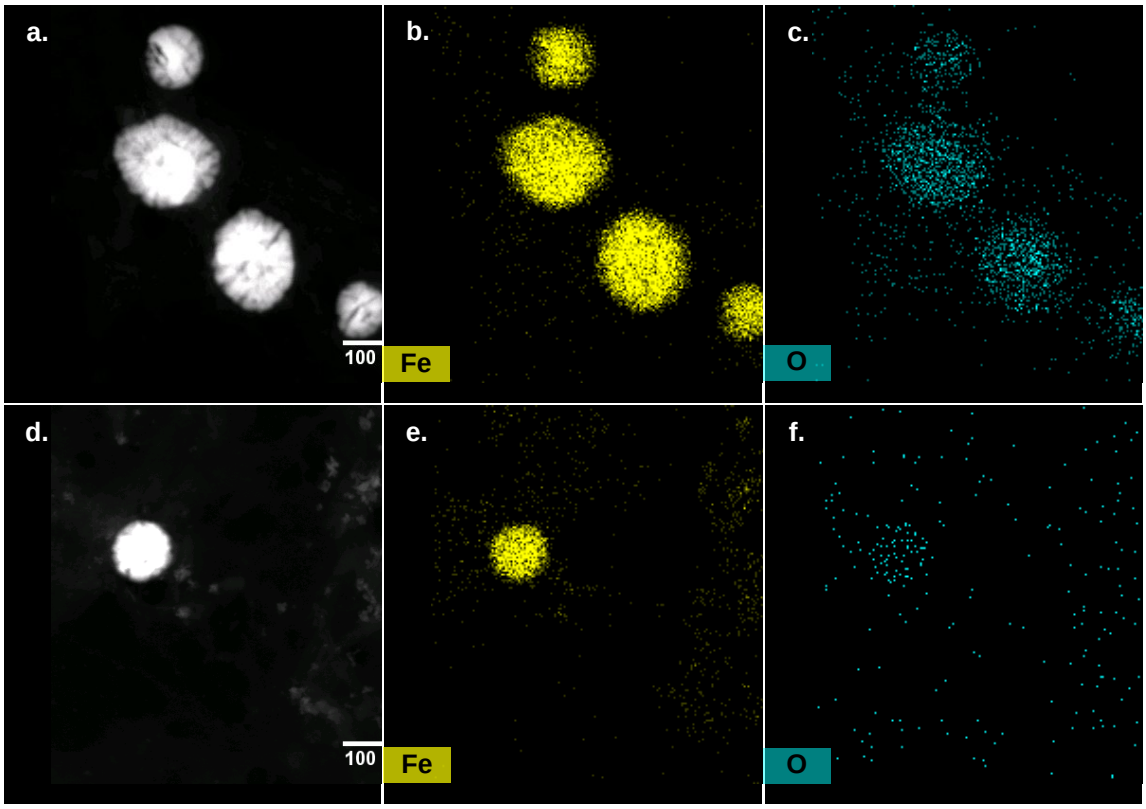

Figure 3.4. Dark field STEM image (a) and EDS maps of CNC:nZVI nanoparticles corresponding to the ratio CNC to nZVI 1:1 diluted in ethanol (top) and water (bottom). STEM images show spherical nZVI in ethanol and in water (a,d). Fe (b,e) and O (c,f) elemental mapping showing the composition of these nanoparticles. The smaller particles formed in water-dissolved samples have the same composition of secondary particles.

3.4 Discussion

The formation of iron particles from a metallic salt follows the following steps (Scheme 3.2 – 1): Formation of zero valent molecules through redox reduction, homogenous nucleation of metallic iron to form primary particles, growth of primary particles through molecular accretion, particle aggregation and coalescence to form secondary particles, and aggregation of secondary particles to form fractal aggregates of iron [78].

The presence of CNCs affects the rates and mechanisms of iron nucleation, growth, and aggregation. Similar changes were reported by *He and Zhao* using CMC as stabilizer [114]. changes are represented in Scheme 3.2 and are explained below.

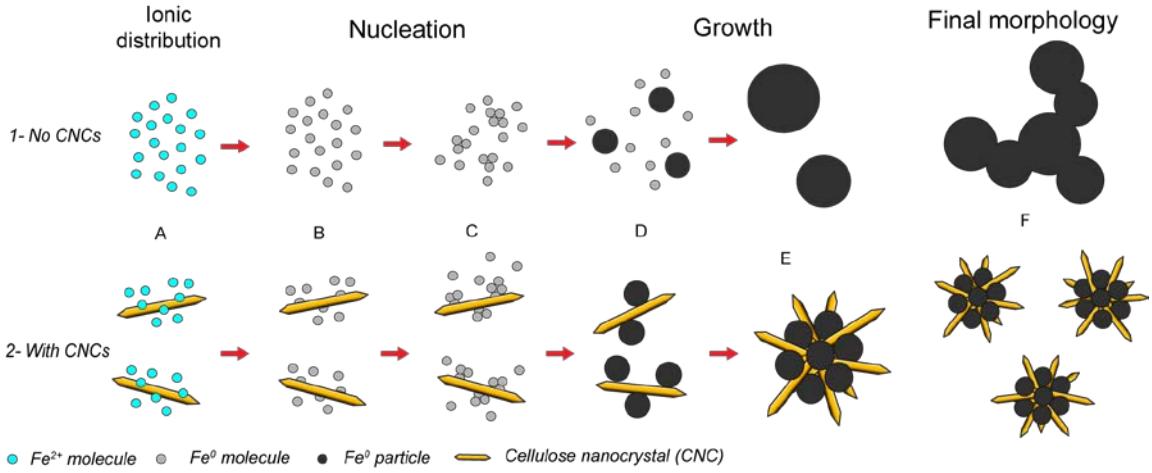

Scheme 3.2. Mechanisms of iron nucleation, growth, and aggregation without (top) and with (bottom) CNCs.

3.4.1 Nucleation and Growth

The sulfate groups introduced during cellulose hydrolysis provide a negative charge over the surface of the CNCs. When a salt is added to an aqueous suspension of CNCs (e.g., $FeSO_4$), cations accumulate at the surface. According to EDL theory, cations form an electric double layer with a positive charge over the surface. The charge distribution of ions decreases as a function of the distance from the surface (Scheme 3.2 - 2A). Following the EDL theory, the distribution of cations decreases exponentially as the distance from the CNCs increases (Eq. 2.). Consequently, redox reactions will preferentially occur at or near the CNC surface when $NaBH_4$ is added. The close proximity of zerovalent iron molecules to the CNC surface encourages the nucleation of metallic iron nanoparticles on the CNC particles (Scheme 3.2 - 2B).

$$n_i(x) = n_i^0 \exp\left[-\frac{z_i e \varphi(x)}{k_b T}\right] \quad \textit{Eq. 2.}$$

n_i: Particle density (#particles/cm^3)

n_i^0: Bulk particle density (#particles/cm^3)

z_i: Ion valency

$\varphi(x)$: Electrical potential energy (V)

k_b: Boltzmann constant (J/K)

e: Charge electron (C)

T: Temperature (K)

The CNC particles initially act as a foreign surface in the liquid phase where the redox reaction occurs. A foreign surface stimulates the nucleation process decreasing the critical free energy required to form a nucleus[78][115]. Under these conditions, an heterogeneous nucleation occurs, which is more favorable than an homogeneous nucleation[116].

A greater concentration of CNCs in solution accelerates the nucleation process due to a higher number of available nucleation sites. After iron nuclei are formed, the iron molecules aggregate on the CNC surface (Scheme 3.2 - 2C) to form primary particles (Scheme 3.2 - 2D). From TEM images, the diameter of those primary particles is ~10nm.

Two steps are involved in the formation of the primary particles: diffusion of the zero valent iron molecules to the nuclei and the adhesion of those molecules to the nuclei [117]. To favor iron nucleation on CNCs over aggregation, we control the rate of iron molecular diffusion by manipulating three variables: the rate of addition of sodium borohydride, the initial iron sulfate concentration, and the CNC concentration. A slow addition rate of sodium borohydride (500µL/min) and a low iron sulfate concentration

(~4mM) results in a low concentration of zero valent iron molecules in the system, and the presence of CNCs increases the viscosity of the solution[118].

Zero-valent iron molecules become zero valent iron nanoparticles on the surface of the CNCs through nucleation and growth. We expect that CNCs do not have a significant impact on the diffusion of zero valent iron molecules. However, the diffusion of the nZVI particles (primary and secondary particles) is impacted by the presence of CNCs because nZVI particles nucleate on the surface of the CNCs and are thereby prevented from aggregating with other nZVI particles. The comparable size of the CNCs and the nZVI particles enables effective stabilization of the nZVI to prevent future aggregation. The presence of CNCs does not have an impact on the cohesive forces between molecules of ZVI and particles of nZVI.

At a critical size at the CNC surface, the primary particles start to interact with one another and grow through aggregation and coalescence[116] to create secondary particles (Scheme 3.2 - 2E). These secondary particles have a mean size of 130nm (Figure 3.2g). The presence of CNCs also affects the growth of primary particles. An increase in the number of CNCs in solution results in a reduction in the rate of diffusion of primary particles and a drop in the rate of aggregation of secondary particles. This statement is evident from the TEM images of fresh iron particles (Figure 3.2). Further, the slower rate of diffusion of primary particles causes less dense, less homogenous secondary particles evidenced by broader size and sphericity distributions of secondary particles (Figure 3.2).

Fractal aggregates observed in bare ZVI are made from secondary particles. CNC particles act as stabilizers to prevent secondary nZVI particles from further aggregation (Figure 3.2e,f). These effects are proportional to the concentration of CNCs in the system

The secondary particles have a surface roughness (Figure 3.2). As described by Baumgartner et al., the roughness indicates that the secondary particles form through primary-particle aggregation rather than molecular accretion[78]. It is likely that primary particles are formed through molecular accretion, while secondary particles are formed from primary particle homoaggregation.

3.4.2 Aging

The size and morphology of the various CNC-nZVI composites is expected to affect the rate and mechanism of nZVI oxidation. To analyze their mechanism of aging, we dissolved nZVI-CNC nanoparticles in two different solvents - DO water and ethanol 60% v/v – and analyzed them under TEM. Ethanol is commonly used to prevent oxidation[18][119] during storage, while iron anaerobically corrodes in water[120]. In Figure 3.3, TEM images show nZVI in more advanced stages of oxidation in water than in ethanol. The reduced concentration of secondary particles and the presence of large numbers of primary particles in water dissolved samples as compared with ethanol dissolved samples suggests that secondary particles degrade to become primary particles in aqueous media, i.e., as a result of aging (Scheme 3.3). The oxide-hydroxide groups formed on the nZVI particle surface during oxidation are more hydrophilic than bare iron. [119]. As the oxide layer grows, there is a strong driving force leading to the break-up of the secondary particles.

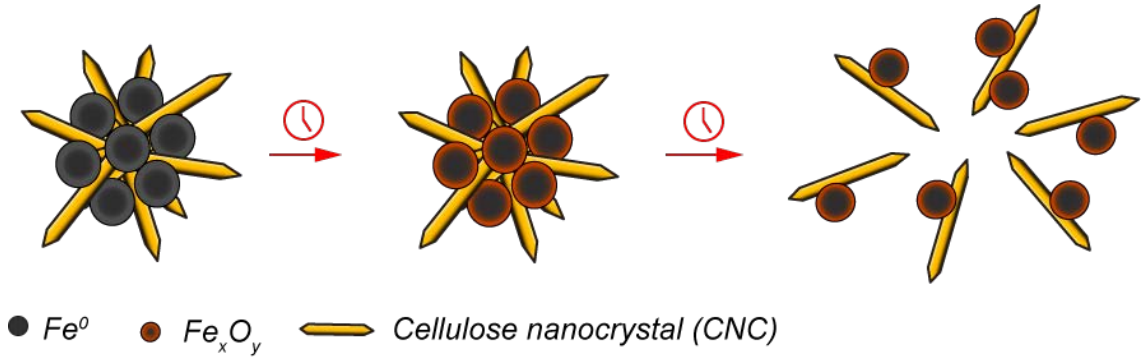

Scheme 3.3 Proposed aging mechanism nZVI particles attached to CNCs

Of importance, both the secondary and primary particles are always attached to CNCs (Figure 3.2e,f, Figure 3.4). This observation implies that the cohesive forces between slightly oxidized primary particles are lower than the adhesive forces between nZVI and CNCs.

Due to the rod-like shape of CNCs with similar dimensions to secondary particles, CNCs do not coat the nZVI surface like other natural biopolymers used in nZVI stabilization [19]. Rather, CNCs acts as a support, leaving a higher surface area available for redox reactions as compared with other organic supports.

3.4.3 Influence of the CNC:nZVI ratio

As shown in Figure 3.2, iron nanoparticles synthesized on CNCs with a ratio of CNC:nZVI of 8:1 have a higher surface roughness and a wider size distribution than nZVI nanoparticles synthesized with fewer CNCs (CNC: nZVI ratios of 1:1 and 4:1). Greater roughness indicates secondary particles composed of less densely packed primary particles, while a broader size distribution is indicative of less uniform aggregation. Therefore, the nZVI in the CNC:nZVI 8:1 system are formed of more loosely packed primary particles than the other two systems. It is expected that higher concentrations of CNCs in solution will further reduce the rate of primary particle aggregation, thereby creating less dense secondary particles. Following this trend,

there may exist a CNC concentration in which primary-particle aggregation is stopped, resulting non-aggregated primary particles as a final morphology. However, at high CNC concentration, CNC homoaggregation occurs, decreasing the surface area available for nZVI nucleation. For this reason, higher amounts of CNC were not evaluated.

Figure 3.1a demonstrates that nZVI is stabilized for all amounts of CNC tested, but the number of particles that are colloidally stable differs within each system. The solution color changes over time from black to light brown and fluffy brown precipitates form (Figure 3.5c). More precipitate forms in the CNC:nZVI 1:1 system (Figure 3.1d) than in the other three systems. This precipitate resembles precipitated magnetite particles reported by Liang et al. [19] when the concentration of their stabilizer was below the critical stabilization concentration (CSC).

In our system, precipitation likely occurs because there are too few CNCs to prevent all the aggregation of secondary particles. While initially all of the nZVI is stabilized by CNCs, some secondary particles are able to aggregate during particle formation. These non-stable CNC-nZVI aggregates were observed to be micrometers in length (Figure 3.5), similar to homoaggregates of nZVI, but clearly composed of primary particles and surrounded by CNCs. Precipitation appears after several days – instead of hours as is observed with raw nZVI – implying that all nZVI are attached to CNCs to some degree and that CNCs stabilize nZVI in solution reducing the rate of sedimentation compared to bare ZVI.

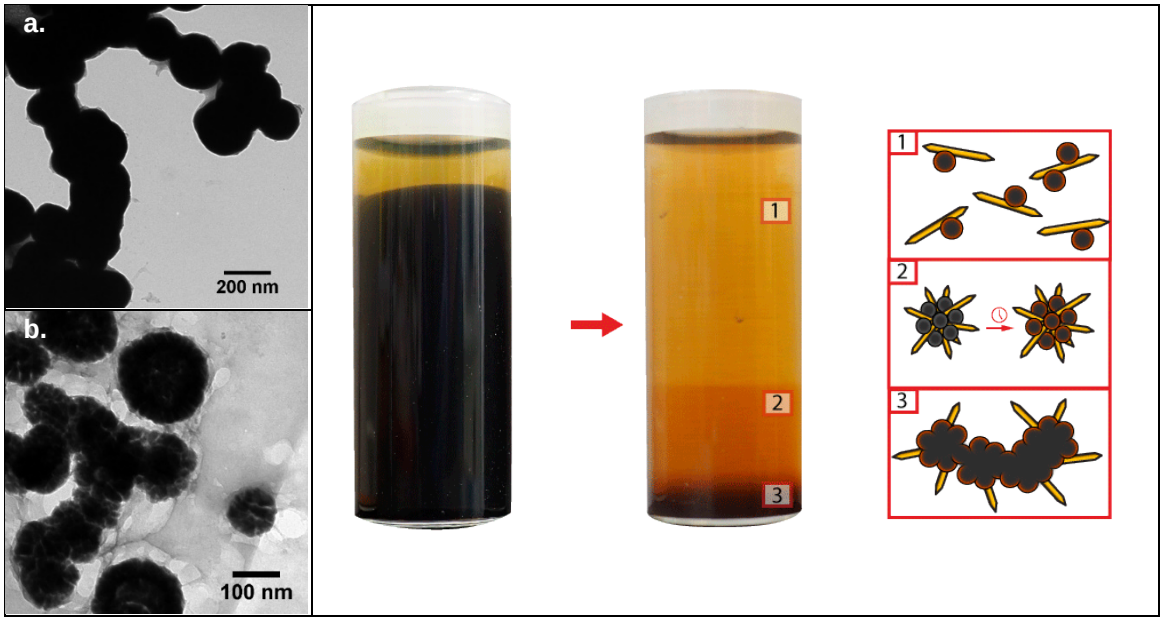

Figure 3.5. (a,b) TEM image of nZVI aggregates without (a) and with (b) CNCs. Fractal aggregates with surface roughness are observed, indicating that CNCs have an impact on the morphology of these structures (c) Vials containing fresh (left) and oxidized (right) iron particles synthesized using CNCs as support with a ratio of 1:1. (d) proposed morphology of CNC- iron particles in each fraction

As seen in Figure 3.1c,d aged vials of CNC-nZVI have vertical gradients of color. These gradients are indicative of both size, density, and oxidation state of the nanocomposites. Black solutions are reduced nanoparticles, while orange solutions are oxidized solutions. The particle density at the top of the vial is lower than at the bottom. The uppermost region is composed of oxidized primary iron particles and other non-spherical morphologies from different iron oxides[67] that form as explained above. As secondary particles break apart during aging, the less dense substructures that form partition to the top of the vial (Figure 3.5-d1), while intact secondary particles remain in the middle. The bottom of the vial corresponds to the particles of CNC-nZVI microscale aggregates that undergo differential settling (Figure 3.5-d3).

The role of CNCs as nZVI stabilizer was quantified by measuring the fraction of suspended particles after 20 days of settling through ICP-OES measurements. The ICP-

OES measurements show that the fraction of iron particles that remain colloidally stable is proportional to the number of CNC particles (Figure 3.1d). As expected, a higher CNC: Fe ratio results in a higher fraction of colloidally stable iron, which supports the hypothesis that the uppermost region of the solutions is composed of a large number of primary particles suspended by CNCs.

A combination of particle size distribution, mass densities and and certain basic assumptions enlables to determine the number of cellulose naocrystals per number of primary and secondary particles (See supporting information). These calculations show that for the system CNC:nZVI 1:1 there is ~2 CNC particles per primary nZVI particle, and ~2100 CNC particles per secondary nZVI particle; while for the system CNC:nZVI 8:1 there is ~12 CNC particles per primary nZVI particle, and ~23000 CNC particles per secondary nZVI particle. These results suggest that not all the CNCs act as a foreign surface for heterogeneous nucleation. Instead, a higher amount of CNCs increases the probability that heterogeneous nucleation occurs. Moreover, these “excess” CNCs are necessary for the synthesis process of colloidally stable nZVI particles since they have other functions during nZVI formation.

3.5 Conclusions

CNCs can act as effective stabilizers for preparing iron nanoparticles with a high colloidal stability. Varying CNC concentration allows fine control over nZVI particle stability, degree of aggregation, size, and morphology. The mechanisms and rates of nucleation, growth, and aging are all affected by the presence of CNCs. Initially, CNCs acts as a foreign surface to encourage heterogeneous nucleation. At a critical nZVI particle size, CNCs act as capping agents and stabilizers, which control nZVI particle size and avoid the formation of microaggregates. The presence of CNCs significantly decreased the rates of both aggregation and sedimentation of nZVI.

nZVI-CNC nanocomposites are ~130nm flower-like spherical aggregates made from ~10nm iron particles supported by CNCs. Aggregated primary particles create nanometer scale roughness over the surface of the ~130nm spherical aggregates. When exposed to air, CNC-supported Fe^0 oxidation is slowed, such that oxidation occurs several days after being removed from a nitrogen atmosphere. This implies that Fe-CNC nanocomposites maintain their reductive activity in normal conditions for long periods of time.

Additionally, aging analysis suggests that secondary particles disintegrate to become primary particles in aqueous media. These primary particles have a higher surface area per volume ratio than secondary particles, which suggests that Fe-CNC nanocomposites may enhance their reactive potential as they age by exposing greater nZVI surface area.

These nanocomposites have good potential for environmental remediation based on their composition, size, morphology, porosity, and mechanism of aging. On-going and future studies will investigate their dynamic reductive activity towards contaminants in soils and groundwater.

3.6 Acknowledgments

Authors would like to thank Daniel A. Osorio, member of Prof. Cranston research group, Heera Marway, member of the Prof. de Lannoy research group, and Dr. Carla Abarca, member of the Prof. Pelton research group for fruitful discussions. TEM studies were carried out at the Canadian Centre for Electron Microscopy. This work was partially funded by NSERC-Discovery and by McMaster University.

3.7 Appendix: Supporting Information for Chapter 3

System	Phase	Dil. factor
Raw nZVI	Liquid	10
	Total	50
CNC:nZVI 1:1	Liquid	10
	Total	50
CNC:nZVI 4:1	Liquid	50
	Total	50
CNC:nZVI 8:1	Liquid	50
	Total	50

Table S3-1. Dilution factors for ICP analysis.

Assumptions for calculate CNC:nZVI particle-number ratio:

- CNCs have the shape of a right square prism with average dimensions of 135nm×7nm ×7nm[113].
- Primary and secondary nZVI particles are spherical.
- The mass density of CNC is 1.5g/cm^3 (Data from cellulose nanocrystals (CNC) product specification sheet – The university of Maine)
- The mass density of nZVI is 7.87 g/cm^3 (density metallic iron at room temperature)

Results:

System	CNC nZVI 1:1	CNC nZVI 8:1
Average diameter primary nZVI (nm)	10.84 ± 6.93	10.59 ± 5.63
Average diameter secondary nZVI (nm)	122.75 ± 30.08	136.1 ± 32.53
Number ratio CNC: primary nZVI	1.81:1	11.9:1
Number ratio CNC: secondary nZVI	2143:1	23352:1

Table S 3-2. Dimensions and characteristics of nanoparticles involved in nZVI synthesis. The average nZVI diameters represent the average of the Feret diameter obtained for each system through TEM images.

Chapter 4: One-step iron metallization of carboxylated cellulose nanocrystals

Abstract: Nanocomposites composed of carboxylated cellulose nanocrystals and iron (Fe-oxCNC) were prepared through a classical redox reaction of iron sulfate using TEMPO-oxidized cellulose nanocrystals (oxCNCs) as a template and stabilizer. Morphological control over Fe-oxCNC nanoparticles was realized by varying the amount of oxCNC added to the redox process. As the molar ratio between oxCNC and Fe was increased from 1 to 8, the morphology of Fe-oxCNC nanoparticles evolved from rounded iron aggregates supported by cellulose nanocrystals to thin film iron-coatings on cellulose nanocrystals. Transmission electron microscopy (TEM), Inductively Coupled Plasma Optical Emission Spectrometry (ICP-OES), and chemical analyses (EDX, EELS) revealed that oxCNCs were coated by iron. Small changes to the density and type of functional groups on the CNC surface have large impacts on the morphology and the oxidation state of adsorbed iron nanoparticles.

4.1 Introduction

Metallic nanoparticles are structures made of pure metals or their compounds with at least one dimension in the nanoscale. Due to their unique properties, they have broad applications in different fields, such as catalysts, sensing, and nanoelectronics[121]. However, metallic nanoparticles have drawbacks due to their lack of colloidal stability and high inter-particle attractive forces [122]. Organic templates can overcome these disadvantages and be used to design new nanocomposite materials with improved properties. Polymer-metal nanocomposites can be synthesized with enhanced mechanical, electronic and chemical properties over pure metal nanoparticles. The desire for greener chemistries in nanoparticle synthesis has increased research focus in the use of natural biopolymers, such as cellulose, starch, and chitosan, as templates for metallic nanoparticles[123].

Carboxylated cellulose nanocrystals functionalized through TEMPO-mediated oxidation (oxCNC) are one possible support. Cellulose is the most prevalent natural polymer on earth[21], and cellulose nanocrystals (CNCs) are its naturally occurring crystalline nanostructure. The presence of primary and secondary hydroxyl groups on the CNC surface provides many chemical functionalization opportunities[5] such the carboxylation of CNC surfaces using sodium hypochlorite as oxidizing agent[35], [124]. Carboxyl groups can adsorb divalent metal ions by covalent binding[36][37]. This surface functionality has been recently used to increase the density of nanoparticles deposit on the CNC surface[37].

In this article, we study the changes in the morphology of Fe-oxCNC nanoparticles by varying the molar ratios of oxCNC and iron. We analyzed the synthesized particles using Transmission Electron Microscopy (TEM), Energy Dispersive X-ray Spectroscopy (EDS), and Electron Energy Loss Spectroscopy (EELS), while the particle stabilization was monitored visually and quantified using Inductively Coupled Plasma Optical

Emission Spectrometry (ICP-OES) and Dynamic Light Scattering (DLS). Compared to our previous study [Chapter 3], we show the importance of carboxyl functional groups at the CNC surface to control the final iron morphology from flower-like nano-zero valent particles supported by CNCs to oxCNCs coated in nano thin-films of iron oxide. We were able to achieve this unique iron association with oxCNCs through simple changes in conventional methods of metallic salt reduction. This association was achieved without thermal inputs, electrical currents, or the addition of surfactants or additional stabilizers.

4.2 Materials and methods

4.2.1 Materials

Cellulose nanocrystals (CNCs) with 0-2% sulfur content were purchased from the University of Maine as ~98% freeze-dried powder. Carbonate buffer (pH 10.5) was prepared with 0.1 M sodium carbonate (boreal science, 16 mL/ 100 mL of buffer solution) and 0.5 M sodium bicarbonate (boreal science, 4mL/ 100 mL of buffer solution) at room temperature. Nitrogen (>99.999%) was obtained from Air Liquide. The following chemicals were used as received: 2,2,6,6-Tetramethylpiperidine 1-oxyl (TEMPO, 8%, Sigma Aldrich), Sodium hypochlorite (NaOCl, 5.65-6%/ Laboratory-grade, Fisher Chemical), Sodium Bromide (NaBr, 99+%, Alfa Aesar), Iron(II) sulfate heptahydrate ($FeSO_4 \cdot 7H_2O$, ≥98.0%, Sigma Aldrich), sodium borohydride ($NaBH_4$ 98%, Alfa Aesar), and methanol (≥99.8% ACS - BDH - VWR international). Ultrapure water (18.2 MΩ) was used throughout the study.

4.2.2 Surface functionalization of cellulose nanocrystals

TEMPO-mediated oxidation of CNC was performed in a 250mL flask according to literature references with minor modifications [125][126]. Each configuration was synthesized in triplicate as explained below.

In a typical run, 1.5g of cellulose nanocrystals were dispersed either in 150mL of deionized (DI) water or 150mL of the buffer solution with magnetic stirring. Solutions of TEMPO (40mM, 0.1mmol TEMPO/g CNC), and NaBr (0.6M, 15 mol NaBr/mol TEMPO) previously prepared with DI water were added and then magnetically stirred for at least 10 min. NaClO (1 mol NaOCl/ mol AGU unit on CNC) was added dropwise at a constant rate using a syringe pump. Two rates were tested, a slow rate (~350µL/min) and a fast rate (10.5mL/min). The pH was maintained at 10.5±0.3 using two different ways: by adding continuously 0.5 M NaOH solution dropwise (referred to as the "no buffer system") [125], and by using carbonate/bicarbonate 0.1M as a buffer solution at a pH of 10.5 (referred to as the "buffer system") [126]. In both cases, the resultant solution was stirred for 3h to ensure complete mixing of all reactants.

After 3h of reaction, a total of 5 mL of methanol was then added to react with the residual NaOCl, and the pH was decreased below 2 with 0.5M HCl. The oxidized cellulose nanocrystals (oxCNC) were collected by centrifugation at 4500rpm for 15 min. After centrifugation, the precipitate was transferred into dialysis membrane tubes (Aldon Corporation) with a molecular weight cut-off of 14,000 Da. The oxCNC solution was dialyzed against deionized water until the permeate water reached a conductivity of 2 mS/cm^2 after being 24h in contact with the dialysis tube. The dialyzed oxidized CNCs were stored at 4°C without further treatment. The concentration of the solutions was determined through as total carbon through a Total Organic Carbon Analyzer (TOC-L Shimadzu) using a calibration curve of raw CNCs at various known concentrations.

4.2.3 oxCNC Characterization

Infrared spectra were recorded using a Thermo Scientific Nicolet 6700 FT-IR spectrometer equipped with a Smart iTX attenuated total reflectance (ATR) sample analyzer.

The carboxyl content of oxidized cellulose samples was determined by conductimetric titration[35]: aqueous oxCNC samples (~35 mg) were suspended into 15 ml of 0.01 M hydrochloric acid solutions. After 10 min of magnetic stirring, the suspensions were titrated with 0.01 M NaOH. A typical titration curve marked by two breaks is shown in Figure S4-2. Analysis of conductometric titrations was used to determine the carboxyl content. Carboxyl content was defined as the moles of carboxyl groups on the CNC molecules divided by the mass of oxCNC (Eq. 4-1).

$$\text{Carboxyl content}\left[\frac{\text{mmol COOH}}{\text{g CNC}}\right] = \frac{C_{NaOH} \times (V_2 - V_1)}{m_{CNC}}$$

Eq. 4-1

C_{NaOH}: Molar concentration NaOH

V_1: Volume fist break point

V_2: Volume second break point

m_{CNC}: mass CNC

4.2.4 Synthesis of nanostructures.

Iron coated oxCNC (Fe-oxCNC) nanoparticles were prepared by adding oxCNCs instead of raw CNCs in the synthesis method of colloidally-stable zero valent iron nanoparticles (nZVI) [Chapter 3]. A summary of the volumes and concentrations used in the synthesis process is shown in Table 4-1.

For further comparison, raw iron (i.e., without oxCNCs in solution) was also synthesized following the procedure previously described.

System	oxCNC Fe 1:1	oxCNC Fe 4:1	oxCNC Fe 8:1	Raw Fe
Molar ratio (AGU:Fe)	1:1	4:1	8:1	-
Molar ratio (-SO_3H:Fe)	1:19.3	1:4.8	1:2.4	-
Molar ratio (-COOH:Fe)	1:4.5	1:1.1	1.8:1	-
Mass ratio (oxCNC:Fe)	2.77:1	11.07:1	22.13:1	-
Mass oxCNC added (mg)	27.7	110.7	221.4	-
Concentration oxCNC (wt. %)	0.055%	0.221%	0.443%	-
Mass $FeSO_4 \cdot 7H_2O$ added (mg)	49.8	49.8	49.8	49.8
Equivalent mass Fe added (mg)	10	10	10	10
Mass $NaBH_4$ added	15.2	15.2	15.2	15.2

Table 4-1. Summary oxCNC:Fe synthesis experimental parameter values.

The synthesis process of iron-coated oxCNCs is illustrated in Scheme 4.1

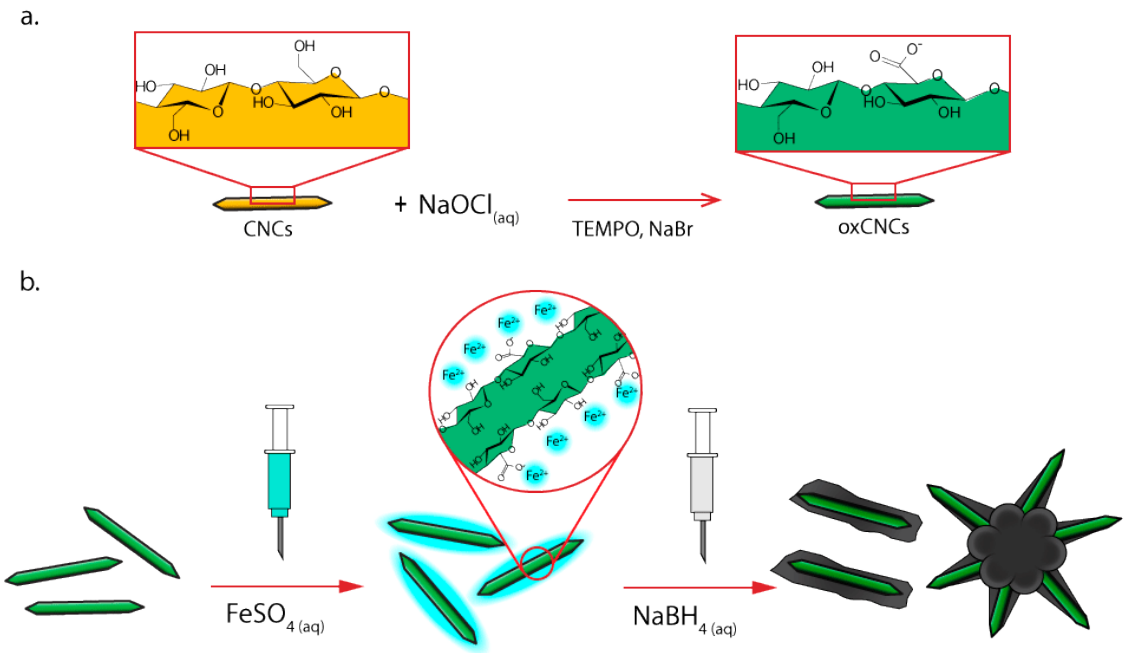

Scheme 4.1. Illustration of iron-coated oxCNC synthesis. a) CNC surface functionalization through TEMPO-mediated oxidation. The primary alcohols at the CNC surface are transformed into carboxylic groups. b) When $FeSO_4$ is dissolved, Fe^{2+} cations interact with the carboxylic groups on the CNC surface through electrostatic attractions and surface complexation. These interactions form an electric layer with a positive charge over the oxCNC

surface. When $NaBH_4$ is added, reduced iron molecules migrate to the oxCNC surface, nucleate and growth forming an iron layer around oxCNCs.

4.2.5 Nanostructure characterization

10mL of fresh nanoparticle suspensions (either raw Fe or iron-coated oxCNCs) were transferred into 10mL vials and kept under lab conditions (22°C, atmospheric pressure), to track their stability over time. The vials were monitored by visual inspection for 1 month and the changes were recorded by photographs. Additionally, the UV-vis spectrum of the Fe-oXCNC nanoparticles were made in a Spark™ 10M multimode microplate reader (TECAN) adding 100µL in a 96-Well UV Microplate.

4mL of fresh Fe-oxCNC nanoparticles were added in a glass vial and were allowed to settle for 20 days under ambient conditions. The amount of sedimented iron was measured using Inductively Coupled Plasma-Optical Emission Spectrometer (Varian Vista Pro ICP-OES) and compared with the total amount of iron added to the vial initially. The iron content was measured at wavelengths of 234.350nm, 238.204nm, 258.588nm, and 259.940nm comparing it with the working standard solutions which were prepared by diluting a multielement standard solution (Sigma Aldrich) on HNO_3 10% w/v. A total of five (5) standard solutions were prepared: 100ppb, 500ppb, 1ppm, 5ppm, 10ppm. The samples were diluted 50-fold in HNO_3 10% w/v.

TEM was used to evaluate the morphology of Fe-oxCNC nanoparticles. The measurements were performed on a Philips CM12 microscope (120 kV). An amount of freshly prepared samples of Fe-oxCNCs nanoparticles were diluted to get a concentration of 100ppm of solids (mass of oxCNC plus iron) before analysis. Methanol was used as solvent to prepare the dilutions. A drop (5 µL, 100 mg/mL in methanol) of the iron-coated oxCNCs dilution was placed on a Holey carbon-coated Copper grid (200 mesh) of 3mm.

The composition of Fe-oxCNCs nanoparticles was investigated using two different techniques: EDX and EELS. EDS analysis was made using a JEOL 2010F microscope equipped with a field emission gun (FEG) operated at 200kV. The system is equipped with a Gatan imaging filtering (GIF) system for the acquisition of electron energy loss spectra. Elemental maps of iron (L2,3 edge: 708 eV, -), oxygen (K edge: 532 eV) and carbon (K edge: 284 eV) were acquired and processed with a Digital Micrograph software provided by Gatan. The grids previously prepared for the TEM images were used for this analysis.

EELS measurements were also recorded on the JEOL 2010F. Spectra were collected at room temperature with a dispersion of 0.3 eV/pixel. The grids previously prepared for the TEM images were used for these analyses.

DLS measurements were performed using a Brookhaven 90 Plus particle analyzer in a scattering angle of 90° at a temperature of 25°C. Every measurement was performed in a plastic UV-vis cuvette at a concentration of 100ppm of solids. Five measurements of one minute each were carried out per sample, with the reported values representing the intensity-weighted mean particle size

4.3 Results

4.3.1 CNC oxidation

Two parameters were modified during the TEMPO-mediated reaction to control the CNC surface oxidation: the rate of addition of the oxidizing agent and the method used for pH adjustment. Binary changes in both parameters provided four configurations to oxidize the CNC surface. These configurations are summarized in Table S4-1, and the results are shown in Figure 4.1

FTIR was used to confirm and characterize the functionalization of the CNC surfaces. The presence of the C=O stretch peak in the range of 1700-1750 indicates the

presence of carboxyl groups[31](Figure S4-1). All oxidized CNCs showed significant FTIR C=O stretching peaks, while no difference was observed between CNCs with different carboxyl content.

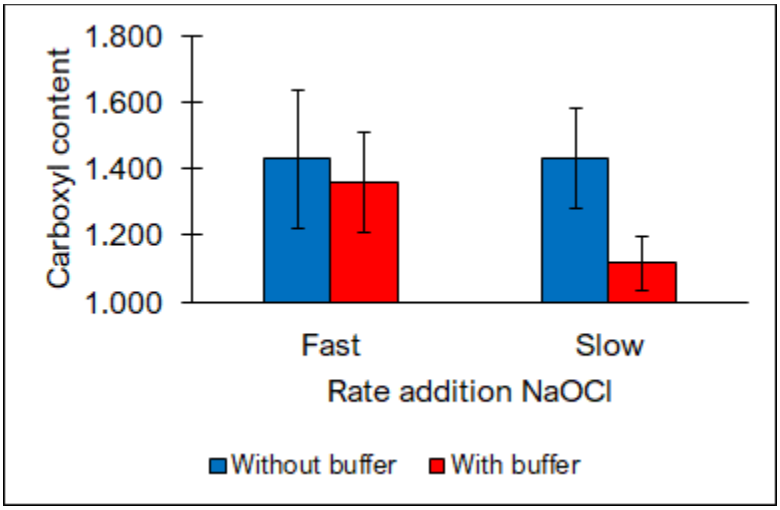

Figure 4.1. Effect of the NaOCl rate of addition and method to adjust pH on the carboxyl content of oxCNCs. Two NaOCl addition rates were tested: a slow rate (~350µL/min) and a fast rate (~10.5mL/min). Error bars represent the standard deviation.

4.3.2 Morphology Fe-oxCNC nanoparticles

Using TEM, we compare the morphology and size of Fe-oxCNC nanoparticles under different amounts of oxCNC in solution. Fe-oxCNC nanoparticles adopt two different morphologies (Figure 4.2a): rounded iron aggregates pierced by oxCNCs (Figure 4.2b) and oxCNCs coated with iron (Figure 4.2c). The characterization of these nanostructures using EDX and EELS confirmed the chemical composition of the iron nanoparticles formed with the oxCNCs (Figure 4.3). Fewer and smaller rounded iron aggregates were observed when the amount of oxCNCs was increased. We used methanol as a solvent for TEM preparation to decrease the rate of iron oxidation and thereby obtain nanoparticles with a higher contrast.

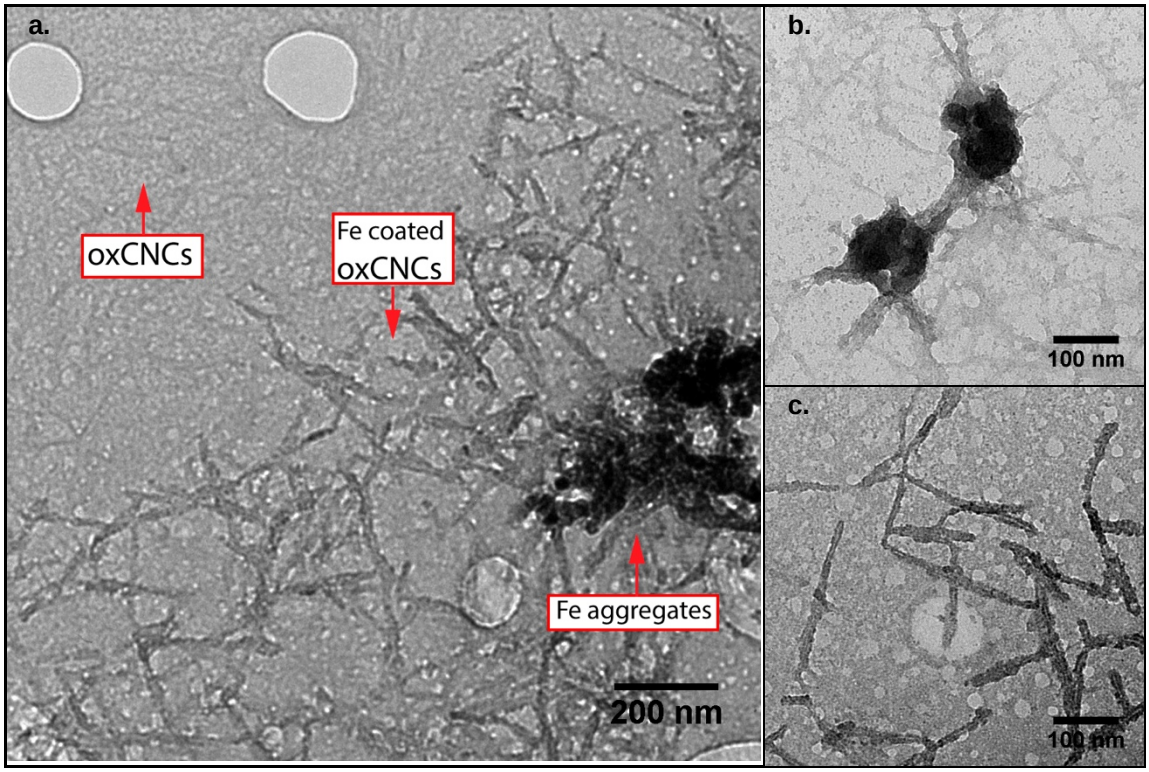

Figure 4.2. TEM images of Fe-oxCNC nanoparticles synthesized with different molar oxCNC to Fe ratios (a, c) oxCNC: Fe 8:1 (b) oxCNC: Fe 1:1. In all solutions regardless of ratio, two types of morphology are observed; coated rods(a, b, c) and aggregates (a,b). The amount of oxCNC in solution has a strong influence on the final morphology of the composite.

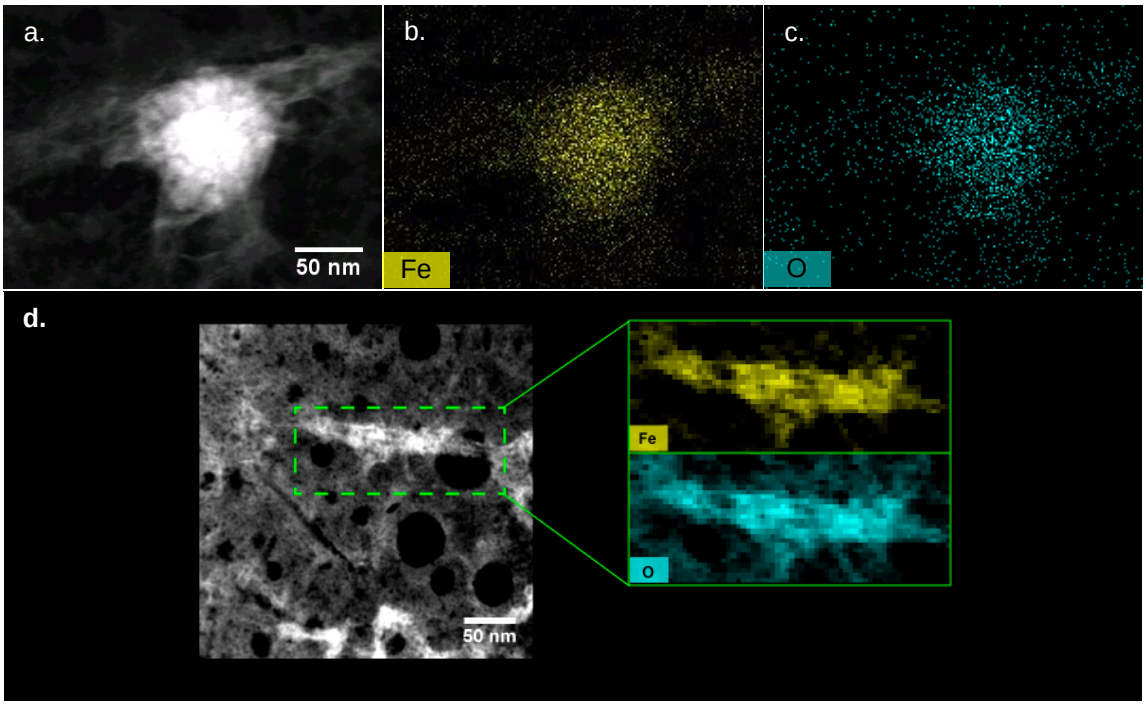

Figure 4.3. (Top) Energy Dispersive X-ray Spectroscopy (EDS) mapping of Fe-oxCNC nanoparticles corresponding to the ratio oxCNC to Fe 1:1. STEM image (a) shows rounded iron aggregates surrounded by iron-coated oxCNCs. Fe (b) and O (c) elemental mapping confirm the composition of these nanoparticles. (Bottom) electron energy loss spectroscopy (EELS) mapping of iron-coated oxCNC nanoparticles corresponding to the ratio oxCNC to Fe 8:1. STEM image (d) shows an isolated iron-coated oxCNC nanoparticle with the same elemental composition obtained for rounded iron aggregates.

4.3.3 Size and Colloidal Stability Fe-oxCNC nanoparticles

Figure 4.4a. shows the visual appearance of Fe-oxCNC nanoparticles in solution after synthesis under normal conditions. The solutions turned from black to orange in a matter of hours without a N_2 atmosphere. Despite rapid oxidation, however, the particles in each vial containing Fe-oxCNCs remain colloidally stable over months. Within one day, there is no noticeable difference between the particles synthesized with different amounts of oxCNC. However, the final appearance of the oxCNC to Fe ratio 8:1 is lighter than the other two ratios tested. This difference in color intensity was corroborated using UV-Vis absorption (Figure 4.4b).

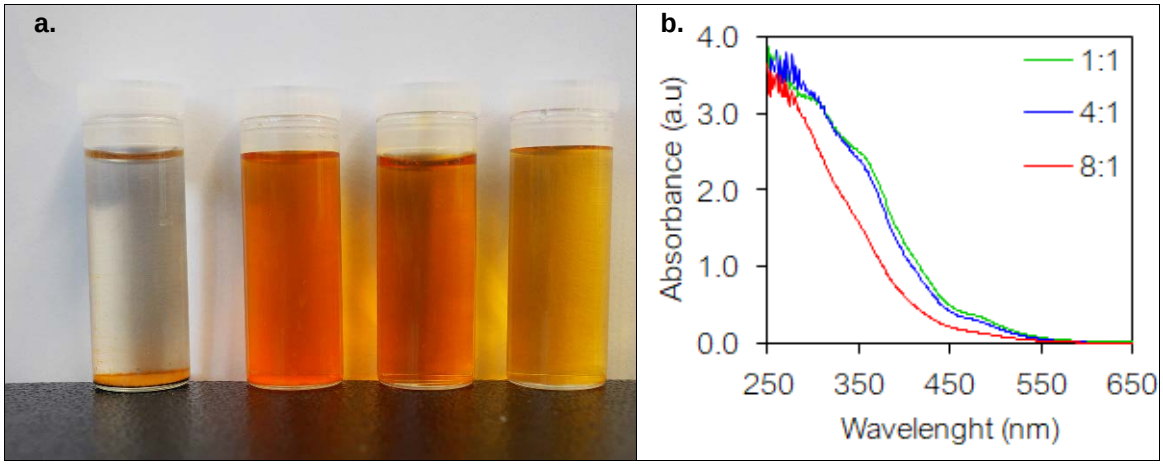

Figure 4.4. (a) Photographs of Fe-oxCNC nanoparticles with different amounts of oxCNC as support (From left to right: Bare Fe, oxCNC: Fe 1:1 - oxCNC: Fe 4:1, oxCNC: Fe 8:1).(b) UV/VIS absorption spectra of Fe-oxCNC nanoparticles.

DLS was used to determine differences in the effective diameter of Fe-oxCNC nanoparticles for each configuration. DLS measurements are a good indicator of the changes in morphology between each system. However, it is critical to note that due to the rod-like shape of CNCs, the effective diameter does not represent any actual dimension of the Fe-oxCNC nanoparticles[127]. Figure 4.5 shows the effect of the number of oxCNCs in solution over the mean diameter. The Fe-oxCNC nanoparticle effective diameter decreases from over 350 nm to less than 120 nm as the oxCNC molar ratio increases from 1 to 4. There is no significant difference between the effective diameter of the systems oxCNC Fe 4:1 and oxCNC Fe 8:1 and these two values are close to the diameter of bare oxCNC particles.

The percentage of sedimented Fe-oxCNC nanoparticles was quantified through ICP-OES measurements. We measure the iron content of the liquid phase on each vial and compare it with the total content of iron. We observe a similar trend to the DLS measurements (Figure 4.5): the percentage of sedimented iron decreases from 15% to 6% as the oxCNC molar ratio increases from 1 to 4, and there is no significant difference

between the percentage of iron sedimented of the systems oxCNC Fe 4:1 and oxCNC Fe 8:1 (6% vs 5%)

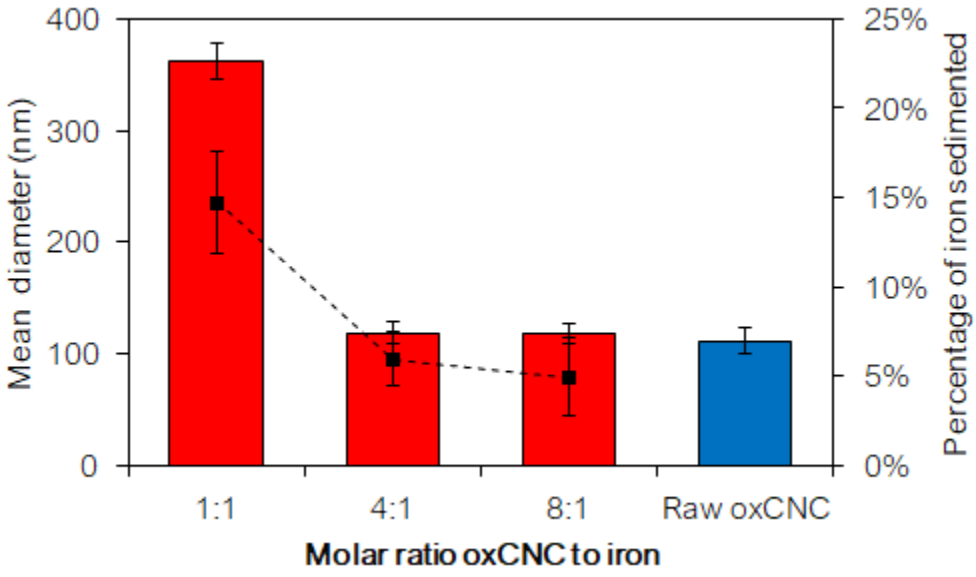

Figure 4.5. Intensity-weighed effective particle diameter(left/bars) and percentage of iron colloidally stable (right/dots) for Fe-oxCNC nanoparticles at different amounts of oxCNC as support. For comparison, the effective particle diameter for oxCNC was also measured. Error bars are the standard deviation.

4.4 Discussion

4.4.1 CNC oxidation.

Figure 4.1 presents the comparison of the oxCNC carboxyl content for CNCs modified for the four different combinations tested. For fast additions of NaOCl, Figure 4.1 indicates that the difference between the two methods to adjust pH -buffer and no buffer- is small and in most cases well within the limits of experimental error. However, the samples synthesized in the presence of a buffer have a lower average degree of oxidation compared with the samples synthesized without a buffer. These differences are more noticeable under the slow rate of NaOCl addition. The addition of a buffer solution increases the ionic strength of the reaction medium. An increase in the ionic

strength results in CNC homo-aggregation[128], leading to a reduction of the primary hydroxyl groups available for oxidation, hence reducing the efficiency of the reaction. The use of a buffer solution is more practical because the necessary pH adjustment is done at the same time as the oxidation. As such, it was determined that a fast rate of NaOCl addition was necessary to achieve the maximum CNC oxidation in the presence of a buffer.

4.4.1 Influence of the molar ratio of oxCNC to Fe

The main difference between the two Fe-oxCNC morphologies obtained (Figure 4.2) is the final form adopted by the iron nanoparticles. The iron-oxCNC morphology is dictated by the iron aggregation mechanism after iron is reduced. Iron molecules can either nucleate on and around oxCNCs or they can homoaggregate. The former leads to iron-coated oxCNCs, while the latter produces spherical nZVI nanoparticles pierced or stabilized by oxCNCs. Iron clusters are further discouraged by using a low iron sulfate concentration in solution (~4mM) and a slow addition rate of sodium borohydride during the synthesis process (500μL/min). Futhermore, during iron-nanoparticle growth, oxCNCs act as capping agents limiting the extend to which iron-nanoparticles grow. A similar effect was observed in our previous studies with raw CNCs [Chapter 3]

The presence of oxCNCs covered by iron oxides is observed in the three EDS measurements (Figure 4.3) In general, Fe-oxCNC nanoparticles without further treatment showed a high dispersion stability with very little aggregation over time. The small amount of precipitation (< 10% of the Fe in solution) likely occurs because there are too few oxCNCs in solution to prevent all iron nanoparticle aggregation. As expected, Figure 4.5 shows that the higher the number of oxCNCs in suspension, the lower the number of iron aggregates.

Non-stable Fe-oxCNC aggregates are micrometers in length (Figure 4.6c), which are similar in structure to homoaggregates of nZVI (Figure 4.6a) and aggregates of Fe-CNC

(Figure 4.6b). The important difference is that the oxCNCs that surround these aggregates clearly show near complete coverage by iron.

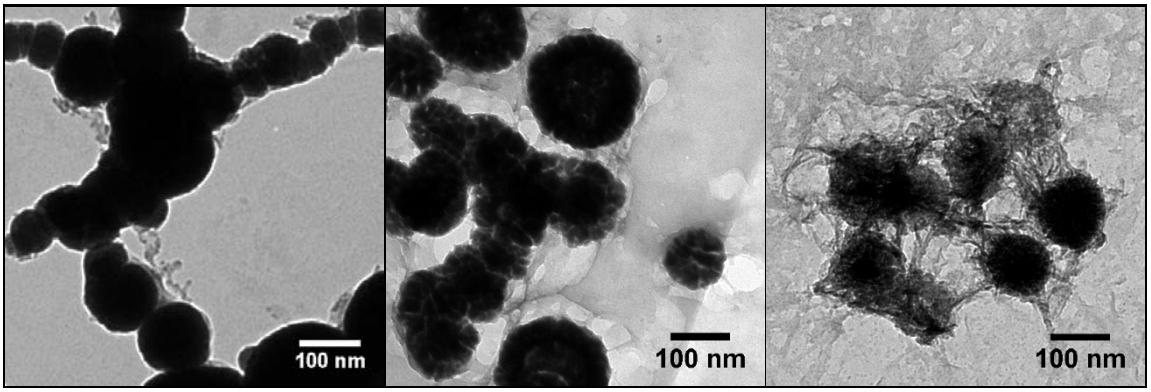

Figure 4.6. TEM images of iron aggregates. From right to left: raw nZVI (i.e. no support). CNC-supported iron aggregates, oxCNC-supported iron aggregates.

4.4.2 Influence of carboxyl groups on Fe-oxCNC morphology

In our previous work [Chapter 3] when we reduced ferrous ions in the presence of raw CNCs, we obtained ~130nm spherical iron aggregates made from ~10nm primary particles. Based on these results, we suggested that the presence of raw CNCs in solution plays a dual role: a foreign surface to encourage stable nucleation over fast aggregation and a stabilizer to prevent iron nanoparticles aggregating into fractal colloids. The presence of oxCNCs also has these effects that led to the formation of stable nanoparticles. However, it was found that the final form of iron oxide nanoparticles is significantly different between these two systems. The carboxylic groups on the CNC surface change the interaction mechanisms between Fe^{2+} and CNCs, which results in a noticeable change of morphology between Fe-CNC and Fe-oxCNC nanoparticles synthesized under the same conditions.

To understand the morphological difference between nZVI-CNCs and Fe-oxCNCs, we consider the impact of functional groups on the oxCNCs. Compared to raw CNCs, carboxyl-functionalized CNCs acquire a higher negative surface charge in normal conditions due to the nature of carboxyl groups: carboxyl groups are more polar than

hydroxyl groups due to the C=O group present on the molecule, and at moderate to high pH values, carboxylic groups ionize slightly by releasing the proton attached to the hydroxyl group. Carboxyl groups increase the repulsive forces between cellulose nanocrystals, hence increasing the stability of CNCs in suspension.

The change of surface potential also has an impact on the number of ions near the oxCNC surface. According to EDL theory, the distribution of ions in solution near a charged surface can be approximated by a Boltzmann distribution (Eq. 2.)[129].

Eq. 2. Indicates that there is an exponential relationship between the particle density and the surface charge of the particle. Comparing the particle density of two surfaces (A, B) with two different surface charges (φ_A, φ_B) we get:

$$\frac{n_{iA}(x)}{n_{iB}(x)} = \exp\left[-\frac{z_i e(\varphi_A - \varphi_B)}{k_b T}\right] = \alpha\exp[(\varphi_B - \varphi_A)] \qquad \textit{Eq. 4-2}$$

Where

$$\alpha = \exp\left[\frac{z_i e}{k_b T}\right] = \exp[77.87 V^{-1}]$$

From Eq. 4-2 is clear that small changes of surface charge will have large impacts on the particle density at the surface, e.g. a difference in 1mV on the surface potential will increase the particle density by ~10%.

A greater impact is likely from the difference in chemical association energy between Fe^{2+} and the functional groups found on CNCs (OH) in comparison to oxCNCs (OH and COOH). It is known that ferrous ions coordinate with carboxylic acids [130]. When $FeSO_4$ is dissolved in a solution containing oxCNCs, the ferrous ions adsorb to the oxCNC surface by binding through the carboxyl groups. This chemical adsorption forms a stronger bond than the electrostatic association of ferrous ions to hydroxyl groups, which occurs in both the CNCs and the oxCNCs.

This new type of interaction between oxCNC and Fe^{2+} increases the amount and proximity of ferrous ions at the oxCNC surface, which causes a rise in the number of Fe^0 nucleation sites when $NaBH_4$ is added. This effect also favors iron nucleation over aggregation. As a result, oxCNCs are covered in a dense thin film of small aggregates that take the appearance of coatings on the oxCNC surface, while single nZVI aggregates form on raw CNCs, which come together to form secondary particles as described previously [Chapter 3]. Due to their size, these small aggregates are quickly oxidized, as is observed in Figure 4.4. Instead of seeing spherical nanoparticles of iron around the oxCNC surface, we observe uniform coatings (Figure 4.2). This visual effect can be explained by the flake and rod morphology that iron nanoparticles adopt after iron is oxidized[67].

When the Fe^{2+} ions are reduced, entropic effects are the main mechanism responsible for the adhesion of Fe^0 molecules. When Fe^0 oxidizes, iron nanoparticles acquire a negative surface charge due to the layer of iron oxide/hydroxides formed on top of the nanoparticle. These new compounds increase the repulsion forces between iron nanoparticles. Moreover, due to their size and colloidal stability, non-coated oxCNCs act as stabilizers of Fe-oxCNC nanoparticles.

4.5 Concluding Remarks

We report the synthesis of colloidally stable Fe-oxCNC nanocomposites through reduction of iron sulfate under N_2 atmosphere. By varying the oxCNC to Fe molar ratio during the one-step redox reduction, it is possible to alter the morphology of Fe-oxCNC nanocomposites from spherical aggregates of ~130nm to individual oxCNCs nearly completed coated in a thin film of metallic iron. The presence of carboxylic groups enhanced the chemical adsorption of iron to the CNC surface leading to the formation of new morphologies. The surface modification of cellulose nanocrystals improved the CNC/iron compatibility and their interfacial adhesion. The number of nucleation

centers and the type of ion-surface bond played an important role over the form of the iron nanoparticles.

4.6 Appendix: Supporting Information for Chapter 4

Sample	Addition NaOCl	Buffer	Carboxyl content
1	Slow	YES	1.07
2	Slow	YES	1.07
3	Slow	YES	1.21
4	Slow	NO	1.37
5	Slow	NO	1.32
6	Slow	NO	1.60
7	Fast	YES	1.44
8	Fast	YES	1.45
9	Fast	YES	1.18
10	Fast	NO	1.63
11	Fast	NO	1.45
12	Fast	NO	1.21

Table S4-1. Configurations tested TEMPO oxidation. Concentration Carbonate/Bicarbonate buffer: 0.1M. Slow NaOCl rate :~350µL/min, fast rate: ~10.5mL/min

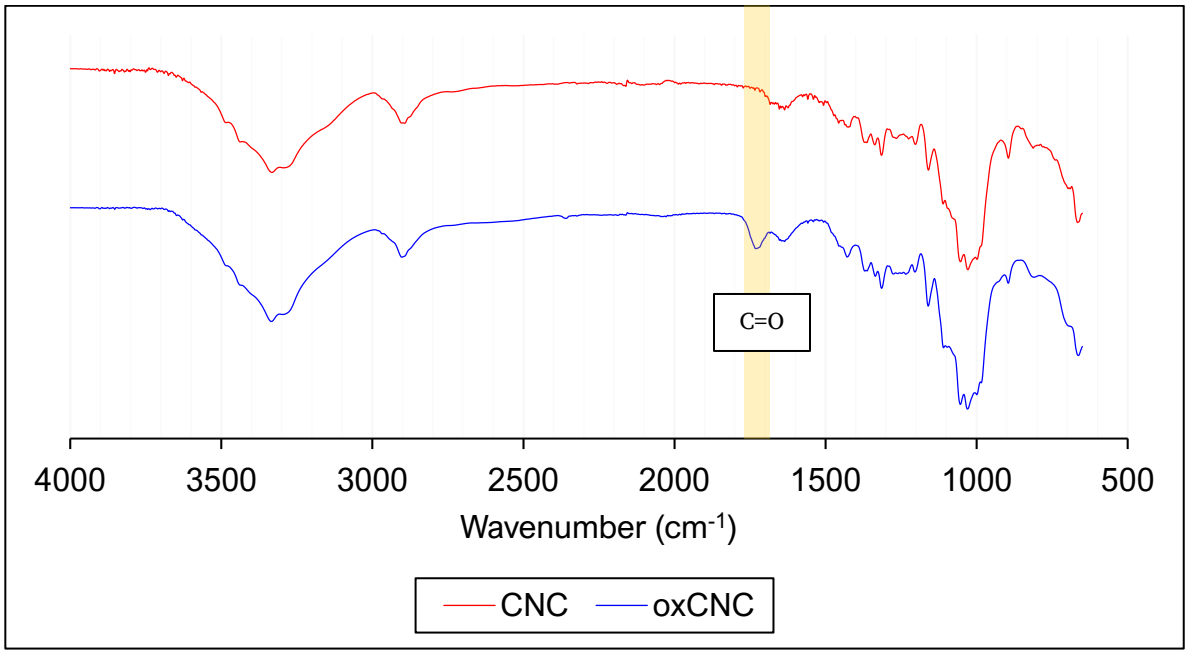

Figure S4-1 FTIR spectra of raw vs. functionalized CNC. Notice the peak (red) in C=O Stretch region.

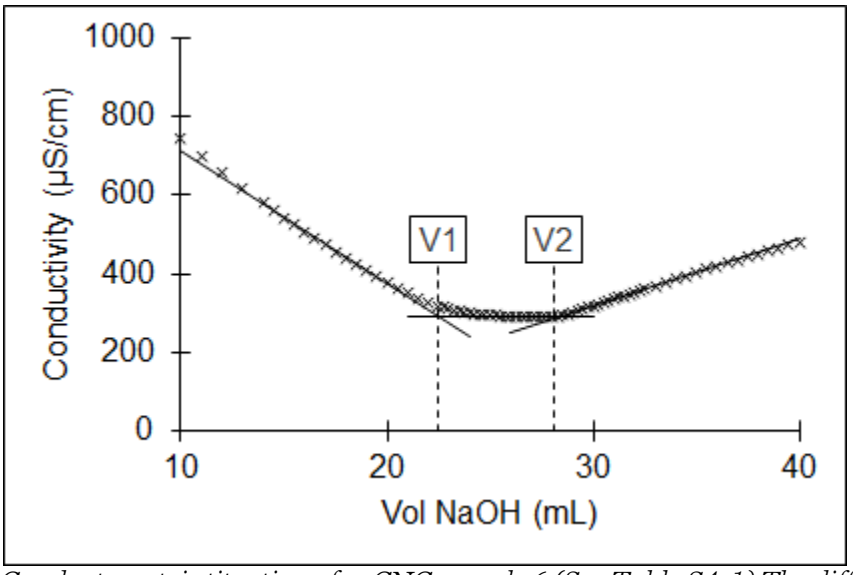

Figure S4-2 Conductometric titration of oxCNC sample 6 (See Table S4-1) The different stages of the titration process can be easily identified[131]*: A rapid decrease in conductivity due to strong acid neutralization, a flat region where neutralization of the carboxyl and sulfate groups on oxCNC surface occurs, and a rise in conductivity due to the excess NaOH added.*

Chapter 5: Conclusions and future work

This thesis has focused a simple method to synthesize colloidally stable metallic iron nanoparticles (FeNPs) by incorporating two different cellulose-based stabilizers: cellulose nanocrystals (CNCs), and carboxylated cellulose nanocrystals (oxCNC). In all experiments, TEM images show that the FeNPs were attached to the stabilizer surface (either raw CNCs or oxCNCs). FeNPs were synthesized through the reduction of the ferrous iron by sodium borohydride ($NaBH_4$) under inert conditions, so its expected that all the particles formed were initially composed by iron in its zero valent state (nZVI).

CNCs and oxCNCs were able to overcome metallic and magnetic attraction forces of Fe0, yielding highly colloidally stable iron nanoparticles.

The FeNPs stability, degree of aggregation, size and morphology can be controlled by manipulating the type and concentration of the stabilizer. These changes are more evident for the iron nanoparticles synthesized using oxCNCs as support.

Both stabilizers perform similar functions along the iron nanoparticle synthesis through chemical reduction of iron sulfate. Initially, ferrous ions were coupled on the CNC surface by electrostatic interactions, and in the case of oxCNC, electrostatic interactions and ligand binding through carboxylic groups. CNCs and oxCNCs change the distribution of Fe^{2+} irons on solution. This new arrangement increases the number of active nucleation sites when $NaBH_4$ is added. Later, during the stages of growth, CNCs and oxCNCs act as (1) template for the formation of Fe^0 seeds on the support surface, (2)capping agent, controlling iron nanoparticle size, and (3) stabilizer inhibiting iron nanoparticle aggregation.

It was observed that the morphology of iron nanoparticles is significantly different between these two supports.

Fe-CNC nanocomposites are ~130nm flower-like spherical aggregates made from ~10nm iron particles supported by CNCs. Aggregated primary particles create nanometer scale roughness over the surface of the ~130nm spherical aggregates. We observed Fe^0 oxidation only occurs several days after being removed from nitrogen atmosphere, meaning that Fe-CNC nanocomposites maintain their reductive activity in normal conditions for long periods of time. Additionally, aging analysis suggests that secondary particles disintegrate to become primary particles in aqueous media. These primary particles have a higher surface area per volume ratio than secondary particles, which makes Fe-CNC nanocomposites more attractive for applications involving surface interaction. The composition, size, morphology, porosity, and mechanism of aging of this type of nanocomposite have a great potential for environmental remediation.

Fe-oxCNC nanocomposite morphology varied from spherical aggregates of ~130nm to individual oxCNCs nearly completed coated in a thin film of metallic iron made from primary particles. By simply varying the surface functional groups, the primary-particle aggregation can be controlled, resulting in non-aggregated iron primary particles. These nanocomposites oxidize in a matter of hours, meaning that resultant iron particles are too reactive to be useful for in-situ environmental applications. However, the proposed approach of carboxylic group surface functionalization with and a subsequent reduction of metallic ions offers a novel approach to synthesizing cellulose-metal composites in aqueous media without applying high temperatures, electrical current, or the use of additional chemicals.

5.1 Future work

It is necessary to make technical improvements in preparing Fe-cellulose nanocomposites to improve the control over FeNP morphology and colloidal stability. Parameters such as the rate of addition of $NaBH_4$, mixing technique employed, and

overall $FeSO_4$ concentration can be modified to optimize the proposed synthesis process without the use of additional chemicals.

Fe-CNCs nanocomposites hold the potential to be used as a cost-effective technology for in-situ soil remediation. For this reason, it is necessary to evaluate the following characteristics: The Fe-CNC capacity in treating a variety of contaminants and compare it with commercial nZVI particles; the influence of temperature, ionic strength, and pH in Fe-CNC colloidal stability; and the Fe-CNC transport in porous media and simulated soils. Also, the use of a greener reducing agent (instead of $NaBH_4$) may also be explored to make this process more sustainable. For example, in last years several authors have been using extracts from natural products(e.g black tea-, grape marc-, and vine leaves [132]) to reduce iron salts.

In the case of Fe-oxCNC nanocomposites, this technology opens the option of using carboxylated cellulose nanocrystals as a template for a variety of metals and metal oxides. Likewise, the presence of other functional groups at the CNC surface that can be attached through more environmentally friendly procedures (e.g. CNC surface acetylation) must be evaluated.

Finally, studies for synthesizing nanoparticles made from inorganic compounds with high value must be addressed. In our research group, we want to target versatile inorganic compounds that can be produced through redox reactions (e.g. Zinc Oxide, Iron (III) oxide, Aluminium oxide) and analyze the influence of the use of CNC as support on the size, morphology, and reactive activity of metal/metal-oxide nanoparticles. Inorganic nanoparticles synthesized on CNCs may reduce the need for purification stages or the use of organic solvents that are hazardous to the environment.